Alloying of 2D Anisotropic Materials and Studying Their Vibrational and Optical Properties

By

Ashutosh Agarwal

A Thesis Presented in Partial Fulfillment
of the Requirements for the Degree
Master of Science

Approved March 2018 by the
Graduate Supervisory Committee:

Sefaattin Tongay, Chair
Matthew Green
Houlong Zhuang

ARIZONA STATE UNIVERSITY

May 2018

ABSTRACT

Alloying in semiconductors has enabled many civilian technologies in optoelectronic, photonic fields and more. While the phenomenon of alloying is well established in traditional bulk semiconductors, owing to vastly available ternary phase diagrams, the ability to alloy in 2D systems are less clear. Recently anisotropic materials such as ReS_2 and TiS_3 have been extensively studied due to their direct-gap semiconductor and high mobility behaviors. This work is a report on alloys of ReS_2 & $ReSe_2$ and TiS_3 &$TiSe_3$.

Alloying selenium into ReS_2 in the creation of $ReS_{2x}Se_{2-x}$, tunes the band gap and changes its vibrational spectrum. Depositing this alloy using bottom up approach has resulted in the loss of crystallinity. This loss of crystallinity was evidenced by grain boundaries and point defect shown by TEM images.

Also, in the creation of $TiS_{3x}Se_{3-x}$, by alloying Se into TiS_3, a fixed ratio of 8% selenium deposit into TiS_3 host matrix is observed. This is despite the vastly differing precursor amounts and growth temperatures, as evinced by detailed TEM, EDAX, TEM diffraction, and Raman spectroscopy measurements. This unusual behavior contrasts with other well-known layered material systems such as MoSSe, $WMoS_2$ where continuous alloying can be attained. Cluster expansion theory calculations suggest that only limited composition (x) can be achieved. Considering the fact that $TiSe_3$ vdW crystals have not been synthesized in the past, these alloying rejections can be attributed to energetic instability in the ternary phase diagrams estimated by calculations performed. Overall findings highlight potential means and challenges in achieving stable alloying in promising direct gap and high carrier mobility TiS_3 materials.

I dedicate this work to my mother, father, brother, girlfriend and my entire extended family.

Without their love and support, I would not have become the first graduate in our family.

ACKNOWLEDGMENTS

I would like to express my sincere appreciation for my advisor and mentor, Dr. Sefaattin Tongay, for including me in his group and letting me work on cutting edge research in the facilities he maintains. His boundless knowledge in the field of 2D materials and science has eased my journey as a master's student. I cannot think of a better advisor to have been my guide at Arizona State University.

I would also like to thank all the group members for their much-needed guidance and unceasing assistance on my projects. Not only were you supportive in my research but you also made this journey extremely enjoyable.

I would like to thank various collaborators from ASU for their contribution to my research and for providing me with meaningful results that helped me work more effectively. Special thanks to Mr. David Wright and Dr. Houlong Zhuang for all their assistance.

TABLE OF CONTENTS

Page

LIST OF TABLES vii

LIST OF FIGURES viii

CHAPTER

1 INTRODUCTION 1

1.1 Two Dimensional Layered Materials (2DLMs) 1

1.2 Planar Graphene Analogues 2

1.2.1 Graphene 2

1.2.2 Boron nitride 3

1.3 Non-planar Graphene Analogues 3

1.3.1 Transition Metal Dichalcogenides (TMDCs) 4

1.3.2 Transition Metal Trichalcogenides (TMTCs) 7

1.4 Anisotropic Materials 8

1.4.1 Rhenium Di Sulfide (ReS_2) 8

1.4.2 Rhenium Diselenide ($ReSe_2$) 10

1.4.3 Titanium Tri Sulfide (TiS_3) 11

1.4.4 Titanium Tri Selenide ($TiSe_3$) 12

1.5 2D Alloys: 13

2 SYNTHESIS AND CHARACTERIZATION 15

2.1 Top Down 15

2.1.1 Chemical Vapor Transport (CVT) 15

2.1.2 Micro Mechanical Exfoliation 16

2.2 Bottom Up 17

2.2.1 Chemical Vapor Deposition (CVD) 18

CHAPTER Page

2.3 Raman Spectroscopy 19

2.4 Angle Dependent Raman Spectroscopy 20

2.5 Photoluminescence (PL) 22

2.6 Atomic Force Microscopy (AFM) 23

2.7 X-Ray Diffraction (XRD) 24

2.8 Energy Dispersive Spectrometers (EDS) 25

3 ALLOY OF 1T PHASE OF TMDc ($ReS_xSe_{(1-x)}$) 25

3.1 Introduction 25

3.2 Crystal Structure 25

3.3 Chemical Vapor Transport (CVT) 26

3.4 Chemical Vapor Deposition (CVD) 27

3.5 Atomic Force Microscopy 28

3.6 X-Ray diffraction (XRD) 29

3.7 Energy Dispersive X-ray Spectroscopy(EDX) 30

3.8 Photoluminescence (PL) 31

3.8.1 Temperature and Power Dependent PL 32

3.9 Raman Spectroscopy 33

3.10 Angle Resolved Raman Spectroscopy 36

3.10.1 Exfoliated Flakes 37

3.10.2 CVD Grown Samples 38

3.11 Anisotropic Ratio Comparison Between CVD and Exfoliated Flakes 38

3.12 Loss of Anisotropy in CVD Grown Samples 39

CHAPTER Page

4 ALLOY OF MX_3- $TiS_{3(1-X)}$ Se_{3X} 41
4.1 Introduction 41
4.2 Crystal Structure 41
4.3 Chemical Vapor Transport (CVT) 42
4.4 X-Ray Diffraction (XRD) 43
4.5 Energy Dispersive X-ray Spectroscopy (EDX) 44
4.6 Raman Spectroscopy 45
4.7 Angle Resolved Raman Spectroscopy 47
5 CONCLUSION AND FUTURE SCOPE 49
5.1 Introduction 49
5.2 Growth 49
5.2.1 ReS_2 & $ReSe_2$ 49
5.2.2 TiS_3 & $TiSe_3$ 50
5.3 Characterization 51
5.4 Conclusion 51
5.5 Future Work 52
5.5.1 Preliminary Studies 53
REFERENCES 57

LIST OF TABLES

Table Page

4-1 Full Width Half Maximum of Raman peaks of $TiS_{2.76}Se_{.24}$ and Its Comparison With TiS_3.....46

LIST OF FIGURES

Figure Page

1-1 Schematics of the Structural Polytypes: 2H (Hexagonal Symmetry, Two Layers Per Repeat Unit, Trigonal Prismatic Coordination), 3R (Rhombohedral Symmetry, Three Layers Per Repeat Unit, Trigonal Prismatic Coordination) and 1T (Tetragonal Symmetry, One Layer Per Repeat Unit, Octahedral Coordination) [33] 5

1-2 a] Crystalline Structure of Layered MoS_2 Where the Mo Atom is Sandwiched Between the S Atoms [20] b] Band Structures Calculated From First Principle's Density Functional Theory (DFT) For Bulk and Monolayer MoS_2 [33] 6

1-3 a] Side (Top Two Panels) and Top Views (Bottom Two Panels) of ReS_2 With Distorted 1T Crystal Structure Compared With the 1H Structure of Conventional TMDs [38] b] PL Spectrum of ReS_2 Flakes With Different Number of Layers [38] 9

1-4 a] Schematic Depiction and Crystal Structure of Monolayer ReS_2 Identifying the b-axis [010] Re-chain direction [39, 40] b] Angle Resolved Raman Intensities of Modes III (green squares) and V (purple triangles) in a 4L sample of ReS_2 Presented in a Polar Plot [40] c] Raman Spectrum Taken on Bulk (Blue) and Monolayer (Red) ReS_2 [38] 10

1-5 a] Top View (Inset is Side View) of the crystal Structure of Layered $ReSe_2$ Simulated With the Help of VESTA Software, Formation of Re_4 1D Chains Can Be Clearly Seen [43] b] Raman Scattering Spectra of $ReSe_2$ on a SiO_2/Si Substrate for (a) 10 Layers; (b) 5 Layers, and (c) a Thick Flake [42] c] Angle-Dependent Raman Intensity of ReS_2 Like Peak in $ReSe_2$ [44] d, Chain Direction of $ReSe_2$ 11

1-6 a] Tilted side View of a Typical MX_3 Crystal Structure. A Top View is Shown With the Black Arrows Indicating Adjacent Chain-Like Structures. The Blue Atoms Represent the Transition Metals While the Yellow Atoms Represent the Chalcogen Atoms [49] b] Raman Spectrum of TiS_3 Whiskers

Figure Page

Measured in Ambience at Room Temperature [50] c] Polar Plot of All TiS3 Modes With Mode III at 372 cm^{-1} [49]....12

1-7 Internal E_{mix} and Free F_{mix} Energies of Mixing Per Primitive Cell For the $MoS_2/MoSe_2/MoTe_2$ 2D Alloys. The Width of the Shaded Areas Denotes One Standard Deviation of the Variation in Calculated Energies [53]....14

2-1 a] Typical Schematic of CVT Growth of Crystals b] Two Zone Furnace Used to Grow All the Crystals....16

2-2 Schematic Representation of the Exfoliation Process....17

2-3 a] Typical Schematic For Chemical Vapor Deposition[59] b] CVD system used to grow 2D Films 18

2-4 a] Schematic Identifying Light Scattering After Laser Exposure on a Sample Surface[60] b] Raman Setup Used to Characterize All Our Materials c] Typical Raman Setup Schematic....19

2-5 a] Rotating Stage Under Optical Microscope For Angle-Resolved Raman Measurement b] Normal and Orthogonal Arrangements to Perform Angle Dependent Measurements 21

2-6 a] Different Types of Recombination's in Materials b] Typical Photoluminescence Schematic...22

2-7 a] Setup For AFM Measurement of Piezoelectric Properties of Thin Films Using a metallic Electrode on the Film Surface b] AFM Image of CD Drive 24

2-8 a] Typical XRD Spectrum Showing Information That Can Be Extracted Out b] XRD Working Principal....25

3-1 High Resolution TEM Showing Diamond Like Chain Structure of ReSSe....26

3-2 a] Optical Image of Exfoliated ReSSe Crystal on Si/SiO_2 Substrate b] Typical Schematic of CVT Growth of ReSSe Crystals 27

Figure Page

3-3 a] Schematic of CVD Growth of ReSSe Crystals b,c,d Different Morphology of ReSSe Film Grown by CVD at Different Temperature....28

3-4 a] AFM Image Shown Bilayers of Exfoliated ReSSe Flake b] AFM Image Showing Monolayer of ReSSe Film Grown Using CVD....29

3-5 XRD Spectrum of ReSSe crystal and its comparison with ReS_2 and $ReSe_2$....30

3-6 EDX spectrum Showing Presence of Rhenium, Selenium and Sulfur Atoms in Exfoliated ReSSe Flakes....31

3-7 Band Gap of CVT Grown ReSSe Crystal Using Photoluminescence Spectroscopy....32

3-8 A] Plot Of PL Intensity V/S Power For Resse B] Temperature Dependent PL For Resse Crystal From 77K To 300K....33

3-9 Raman spectrum of Exfoliated ReSSe flakes and Its Comparison With ReS_2 and $ReSe_2$ Raman Spectrum....34

3-10 Thickness Dependent Raman Spectrum of ReSSe....35

3-11 Raman Spectrum of CVD Grown ReSSe Alloy and its Comparison With the CVT Grown ReSSe....36

3-12 Polar Plot of 406 cm^{-1} and 212 cm^{-1} Like ReS2 Peaks of ReSSe....37

3-13 Angle-Dependent Polar Plots of CVD Flake For Domain A (Black), B (Red), And C (Green), D (Blue), E (Purple), And F (Pink) in a Hexagonal Flake....38

3-14 a] Polar Plots Showing Comparison of Anisotropy in Exfoliated v/s CVD Grown Samples b] Box Plot of Anisotropic Ratio Comparison Between Exfoliated and CVD Grown Sample....39

3-15 High Resolution TEM Images Showing Grain Boundaries, Different Domains and Amorphous Region....40

Figure Page

4-1 a] Side View and Top View of Monoclinic Structure of TiS_3 b] Flake of $TiS_{2.76}Se_{.24}$ on TEM Grid c] Diffraction Pattern of $TiS_{2.76}Se_{.24}$ Showing 200 and 020 Directions. 42

Figure 4-2 a] Ampoule Showing $TiS_{2.76}Se_{.24}$ Growth b] Optical Image of Exfoliated $TiS_{2.76}Se_{.24}$ Nanowire on Si/SiO_2 Substrate. C] Typical CVT Growth Setup of $TiS_{2.76}Se_{.24}$ d, $TiS_{2.76}Se_{.24}$ Nano Wire Like Crystals After CVT Growth....43

4-3 Left, XRD spectrum of $TiS_{2.76}Se_{.24}$ and Its Comparison With TiS_3. Right, Zoomed in view of One of the Peak to Show Deviation in $TiS_{2.76}Se_{.24}$ From TiS_3....44

4-4 EDX Spectrum of $TiS_{2.76}Se_{.24}$ Showing Presence of selenium, Sulfur and Titanium 45

4-5 Raman Spectrum of $TiS_{2.76}Se_{.24}$ and Its Comparison With TiS_3....46

4-6 Polar Plot of Raman Active Peaks of $TiS_{2.76}Se_{.24}$ and Its Comparison With TiS_3....48

5-1 Theoretically Calculated Convex Hall Curve For Alloy of TiS_3 and TiSe3, Showing the Most Favorable Composition....51

5-2 a] ReS_2 Grown on the Edges of WS_2 With Chain Direction Perpendicular to the Edges b] Polar Plot of the ReS_2 Showing Chain Direction at the Edge I and II [64] 53

5-3 AFM Images Showing Terraces on Sapphire Substrate, (Right) Shows Zoomed in View of These Terraces 54

5-4 a] Optical Image of CVD Grown ReS_2 on Non-Treated Sapphire Substrate b] Optical Image of CVD Grown ReS_2 on Surface Reconstructed Sapphire....55

5-5 Raman Spectrum of CVD Grown ReS_2 on Surface Reconstructed Sapphire Substrate....55

5-6 a] AFM Image of CVD Grown ReS_2 on Sapphire Terraces b] Polar Plot of ReS_2 Grown on Sapphire Terraces Using CVD....56

Chapter 1 Introduction

1.1 Two Dimensional Layered Materials (2DLMs)

We are at the start of a new revolution eponymously named the Nanotechnology Revolution. The potential of this field lies in tailoring materials, atom to atom, resulting in advancement of autonomous cars, high-performance computing and super-efficient electronics. This technology rise is further supported by a novel class of materials called 2D materials. Discovery of graphene (mono layer of graphite) by Novosolove & Geim in 2004 through scotch tape exfoliation led to an exponential rise in the field of 2D materials [5]. Since then over 800 2D materials have been discovered such as hexagonal boron nitride, black phosphorus & MoS_2 from family of transition metal dichalcogenides, TiS_3 from transition metal trichalcogenides etcetera which will be discussed further [6-8,10]. In contrast to this enthusiasm are some theories that indicate 2D materials are unstable at room temperature due to lattice vibration fluctuation [1-4].

All 2D materials are layered in nature due to Van der Waals interaction between layers and hence classified as Van der Waals solids. Theoretically, layered materials cover many compounds across the periodic table like - chalcogenides, halides, carbides, nitrides, hydrides, hydroxides, phosphates etc. Many of these materials have been demonstrated experimentally and researchers are working towards proving the rest. Intralayer covalent and ionic bonding & weak interlayer Van der Waal bonding make their layered structure easy to exfoliate – mechanically and chemically [5]. Additionally, low electron cloud interaction between layers in Van der waals solid is itself responsible for overall structural stability.

As discussed above, after the discovery of graphene many other 2D materials have been theoretically and experimentally proven. These materials can be broadly classifying into two categories planar graphene analogue and non-planar graphene analogue [9].

1.2 Planar Graphene Analogues

These materials contain single layer with in-plane covalent or ionic bonding. There are many planar analogues in existence such as graphene, hexagonal boron nitride, silicone, BC_3, SiC silagraphene etc. [20]. In this section we will discuss graphene and h-BN.

1.2.1 Graphene

Carbon is the building block of organic chemistry. Due to flexible bonding, carbon allotropes exist in different crystal structures. Among them graphene is the outstanding 2-dimensional system. Graphene is a monolayer of graphite arranged in 2 dimensions. It is an allotrope of carbon in the form of a honey-comb lattice in which one atom forms each vertex [5]. As mentioned above, graphene was first prepared by mechanical exfoliation from graphite by Geim & Novosolove in 2004. After that, it was synthesized by more reliable techniques like liquid exfoliation [14], chemical vapor deposition (CVD) [15] and reduction from graphene oxide [13]. Graphene has completely different properties from its 3D allotrope graphite. It is a zero-band gap semiconductor with large theoretical specific surface area (2630 m^2g^{-1}), high intrinsic mobility (200 000 $cm^2v^{-1}s^{-1}$), high Young's modulus (~ 1.0 TPa) and thermal conductivity (~ 5000 $Wm^{-1}K^{-1}$), optical transmittance (~ 97.7%) and good electrical conductivity. Typically, important properties of graphene are a quantum Hall

effect at room temperature [12], an ambipolar electric field effect along with ballistic conduction of charge carriers, tunable band gap and high elasticity [5, 11]. Even with the outstanding properties, its use is limited in semiconductor industry due to zero band gaps. Many successful studies have been performed for band gap modulation [16-18]. But there is always been some critical property loss during band gap engineering and this led to rise of other 2D materials with definite band gaps.

1.2.2 Boron nitride

Boron nitride nanomaterials are isoelectronic to carbon. Among various polymorphs, an h-BN (hexagonal boron nitride) analogue to graphite is the most stable one. In bulk form h-BN is very similar to graphite with lattice constants of a= 2.545 A, b= 6.69 A for graphite and a= 2.5 A, b= 6.66 A. Because of this similarity, monolayer of graphene is called as white graphene [9, 19]. Like graphene many synthesis methods have been reported, among them controlled CVD is most feasible to achieve large area growth [22-23]. Despite structural similarity h-BN is highly insulating as compared to zero band gap graphene with direct band gap of 5.9eV [21]. Also, it is thermally and chemically more stable with excellent thermal, chemical and optical properties. Owing to large band gap in UV region, h-BN is an ideal material for diverse applications including dielectric materials and ultra violet laser devices.

1.3 Non-planar Graphene Analogues

In contrast to planar graphene analogue materials, non-planar analogues have layered structure with metal atoms sandwiched between 2 or 3 layers of chalcogen atoms in TMDCs and TMTCs respectively.

1.3.1 Transition metal dichalcogenides (TMDCs)

Despite its high carrier mobility, Graphene, due to its semi metallic nature is not suitable for FET's. Transition metal dichalcogenides (TMDCs) equipped researchers with next generation 2D semiconductors having finite band gap and theoretical carrier mobility of 200 $cm^2/V/s$. Layered TMDCs have generic formula MX_2, where M stands for metal and X stands for chalcogens. The intralayer interaction is covalent in nature while interlayer interaction is held by Van der waals force, making them easier to cleave [9,24]. TMDCs synthesis is like graphene due to same surface energy of both the materials. Generally used method is micromechanical cleavage and chemical vapor deposition [9]. The phase in TMDCs is dominated by d-electrons counts. These are predominantly found in three polymorphs called 1T, 2H and 3R as shown in figure 1-1. Where c-axis defines out of the plane and a & b-axis defines in-plane coordinates. Number in prefix signifies the no. of layer for unit cell and letter indicates the symmetry, T-trigonal, H-hexagonal, and R-rhombohedral. Based on the crystal structure these materials are broadly classified into Isotropic and Anisotropic materials. We will discuss anisotropic materials in next section.

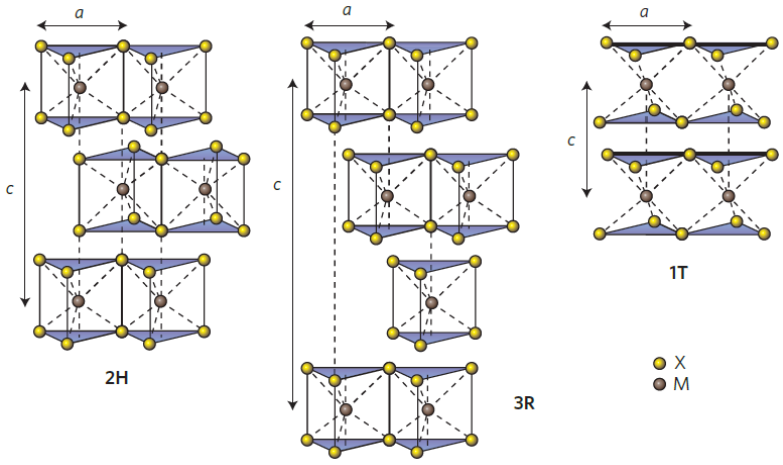

Figure 1-1 Schematics of the structural polytypes: 2H (hexagonal symmetry, two layers per repeat unit, trigonal prismatic coordination), 3R (rhombohedral symmetry, three layers per repeat unit, trigonal prismatic coordination) and 1T (tetragonal symmetry, one layer per repeat unit, octahedral coordination) [33]

These materials exhibit unique properties like direct band gap, better mechanical and electronic properties which make them the most interesting candidate for the study of high tech electronic, optoelectronics, DNA sequencing, energy devices. Despite having similar structure, properties of TMDCs vary from metal to semiconductor all the way to insulator. The band structure of these materials changes a lot from bulk limit to monolayer, from indirect to direct band respectively because of quantum confinement effect. There are about sixty number of TMDCs at present and about two third are layered. In this section we will only discussed the most widely known 2D molybdenum disulfide.

3.1.a MoS_2

MoS_2 is layered TMDCs with S-Mo-S covalently bonded and weakly bonded to other layers by Van der Waal forces [25]. These Van der Waal forces allowed MoS_2 to form in three different polymorphs which differs in stacking sequencing and coordination number. The

2H and 3R phase of MoS_2, both have trigonal prismatic coordination with 2H has hexagonal and 3R has rhombohedral symmetry. Also, the 1T phase is synthetic form of MoS_2 has octahedral coordination and tetragonal symmetry. MoS_2 is an indirect band gap semiconductor in bulk with the band gap of 1.2 eV which transitioned into direct band gap of 1.9eV in monolayer regime as shown in figure 1-2b [26].

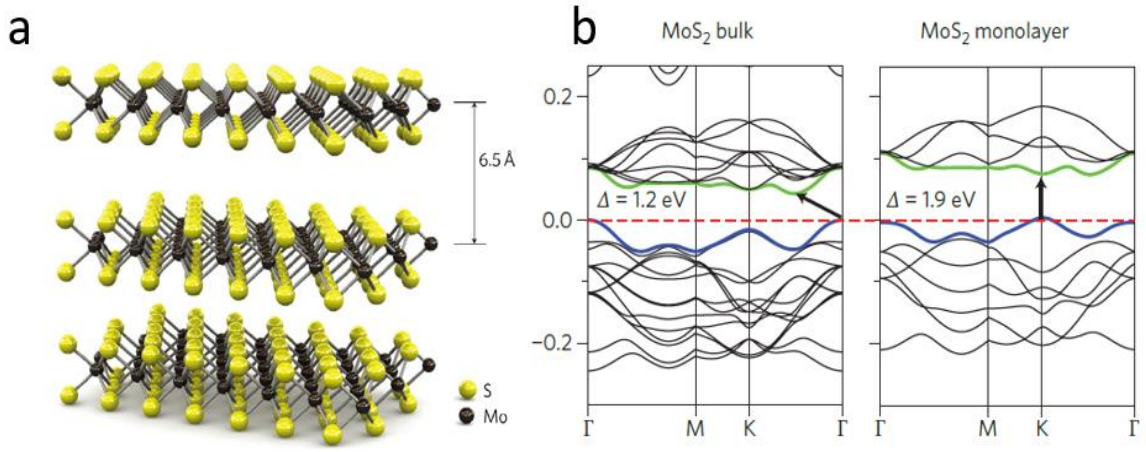

Figure 1-2 a] Crystalline structure of layered MoS_2 where the Mo atom is sandwiched between the S atoms [20] b] Band structures calculated from first principle's density functional theory (DFT) for bulk and monolayer MoS_2 [33]

Yield stress and young's modulus of monolayer MoS_2 is predicted to be 17.5 $N.m^{-1}$ and 170 GPa by first principal calculation [27] which is comparable to graphene. Also, high carrier mobility (~200 $cm^2/V/s$), high on/off ratio (>10^{10}), immunity to short channel effect (drain induced barrier lowering~ 10mV/V) and abrupt switching make it one of the most attractive materials for field effect transistors [28]. It is also one of the best materials for flexible electronics, as it is 30 times stronger than steel can be deformed up to 11% before breaking. Due to its unusual but interesting properties, it has been widely used in other research fields

such as catalyst in dehydrosulfurization [29], dry lubricant [30], photocatalyst [31], lithium ion batteries [32], DNA sequencing, molecular sensing application etc.

With advanced studies, carrier mobility for MoS_2 based FET was corrected to be 15 $cm^2/V/s$ [34]. The low mobility value does not affect FETs properties. This is because transport mechanism for less than 10nm node applications is governed by ballistic process rather than scattering. Still, high mobility is desired in other applications such as RF transistors etc. This propelled the research on transition metal trichalcogenides.

1.3.2 Transition metal trichalcogenides (TMTCs)

TMTCs are new class of materials akin to TMDCs with novel properties. TMTCs (MX_3) are composed of either group-IVB or group-VB transition metals (M) and chalcogen atoms (X = S, Se, or Te). Molybdenum and tungsten trichalcogenides have also been synthesized but turn out only to be amorphous [35]. Mostly TMTCs possess monoclinic structure with two almost similar variants, $ZrSe_3$ type and TiS_3 type with $P2_{1/m}$ space group [36]. Each layer is held together via quasi 1D structure that can be viewed as triangular prism in MX_6 unit along b-axis [36]. This quasi 1D properties from reduced in-plane symmetry makes this class of materials highly anisotropic.

Since these are the newest class of materials, theory is currently ahead of experimentation. As per the theory, all the materials except 2D TiS_3 are metallic or indirect band gap semiconductors. Among them $TiTe_3$, $ZrTe_3$ and $HfTe_3$ are metallic and $TiSe_3$, ZrS_3, HfS_3, $ZrSe_3$and $HfSe_3$ are indirect band gap semiconductor ranging from .57eV to 1.92eV. In general, if we look at group IV, TMTCs are mostly semiconducting except Te. In group V we see mix phases such as charge density waves and super conductivity, for

example NbS_3 show resistive anomalies at 340K, and $NbSe_3$ at 145K, 59K. Also, $TaSe_3$ shows superconductivity transition at 2.1K. [37]

Because of band gap being closer to silicon and anisotropic nature, these materials can be used in various fields. Such as fabrication of next generation high mobility transistors, generation and detection of polarized light i.e. on chip polarizers, polarization sensitive photodetectors and in lithium ion batteries. [36]

1.4 Anisotropic Materials

Anisotropic or pseudo one dimensional materials are new class of materials with direction dependent properties. The in-plane atoms of these materials arrange themselves in such a way that they form chain-like structures extending along a given lattice direction which leads to strong anisotropic behavior. In these materials electron phonon interaction with photon behave anisotropically. Due to this, the materials mechanical, electrical and optical property behave differently in different directions. Some of the most prevalent examples of pseudo 1D materials are black phosphorus, ReS_2 & $ReSe_2$ from TMDCs and TiS_3 from TMTCs. Anisotropic materials have huge potential in many device applications like polarizers, FET, photo detectors etc.

1.4.1 Rhenium di sulfide (ReS_2)

ReS_2 is a layered group V transition metal dichalcogenides with two sulfurs covalently bonded to rhenium atom and bonded to other layers by Van der Waal force. This material is different from other TMDCs as band renormalization is absent and bulk ReS_2 behaves

exactly same as monolayer ReS_2. Such unique response originates from lack of interlayer registry and weak interlayer coupling arising from Peierls distortion of the 1T structure of ReS_2. As a result, ReS_2 remains a direct band gap semiconductor even in bulk form as shown in figure 1-3 b. Figure shows that ReS_2 is stable in distorted octahedral 1T shape as compared to 1H stable phase of majority of other TMDCs. This distorted shape leads zigzag Re chains along one of the lattice vectors in the plane. This zigzag chain along one direction shown in figure 1-4a leads to direction dependent properties. ReS_2 chain direction can be identified using angle dependent Raman spectroscopy. Owing to low symmetry ReS_2 possess large number of Raman peaks as shown in figure 1-4c. [38]

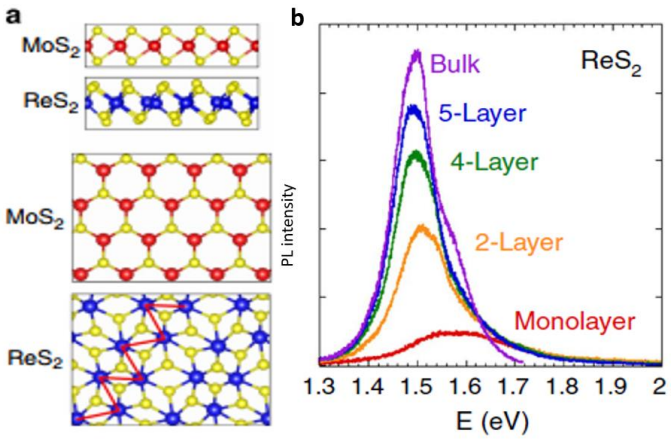

Figure 1-3 a] Side (top two panels) and top views (bottom two panels) of ReS_2 with distorted 1T crystal structure compared with the 1H structure of conventional TMDs [38] b] PL spectrum of ReS_2 flakes with different number of layers [38]

Peaks from 139 cm^{-1} to 312 cm^{-1} mostly comes from E_g (in plane) and A_g (out of plane) like mode [38]. Peaks from 130cm^{-1} to 230cm^{-1} is related to rhenium atom vibration and after that is mainly related to sulfur vibrations [38]. Fifth lowest frequency 213cm^{-1} describes

the atomic displacement of Re-Re bond. The integrated intensity of this peak is maximum when the laser polarization is parallel to Re chains which is named as b-axis as shown in figure 1-4b.

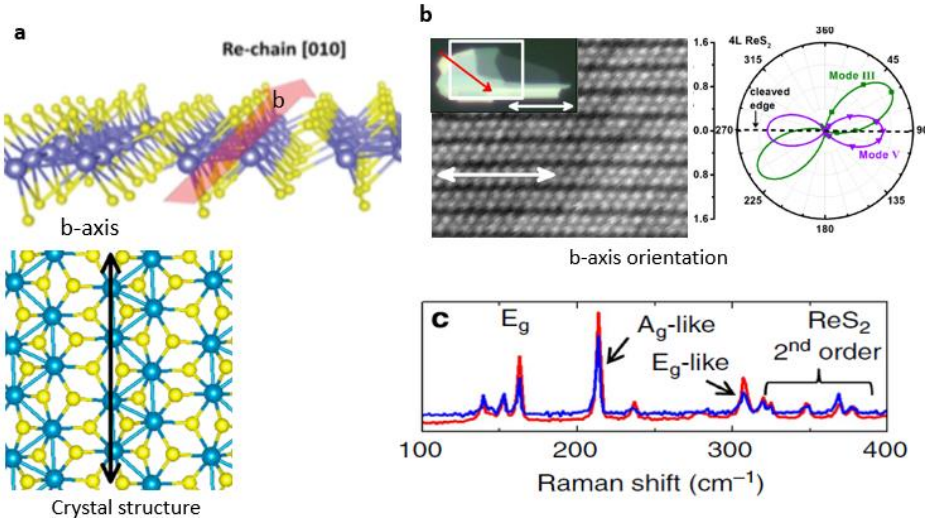

Figure 1-4 a] Schematic depiction and crystal structure of monolayer ReS_2 identifying the b-axis [010] Re-chain direction [39, 40] b] Angle resolved Raman intensities of modes III (green squares) and V (purple triangles) in a 4L sample of ReS_2 presented in a polar plot [40] c] Raman spectrum taken on bulk (blue) and monolayer (red) ReS_2[38]

1.4.2 Rhenium diselenide ($ReSe_2$)

On the other hand, $ReSe_2$ is indirect band gap layered semiconductor material with band gap of 1.26eV [41]. Like ReS_2, $ReSe_2$ also crystallizes in 1T octahedral structure with triclinic symmetry [41]. Electronic and vibration coupling is also absent in this material as shown due to peirels distortion. $ReSe_2$ also exhibit in plane anisotropy with 1D chain of Re atoms arranged in Re_4 diamond shape along b-axis as shown in figure 1-5 a, d. Raman spectrum of $ReSe_2$ is shown in figure1-5b, peaks from 130cm^{-1} to 180cm^{-1} is related to rhenium vibrations

and after that it is related to selenium vibrations. 172cm^{-1} peak is corresponding to mode V peak in ReS_2 and used to identify the rhenium chain direction as shown in figure1-5c.

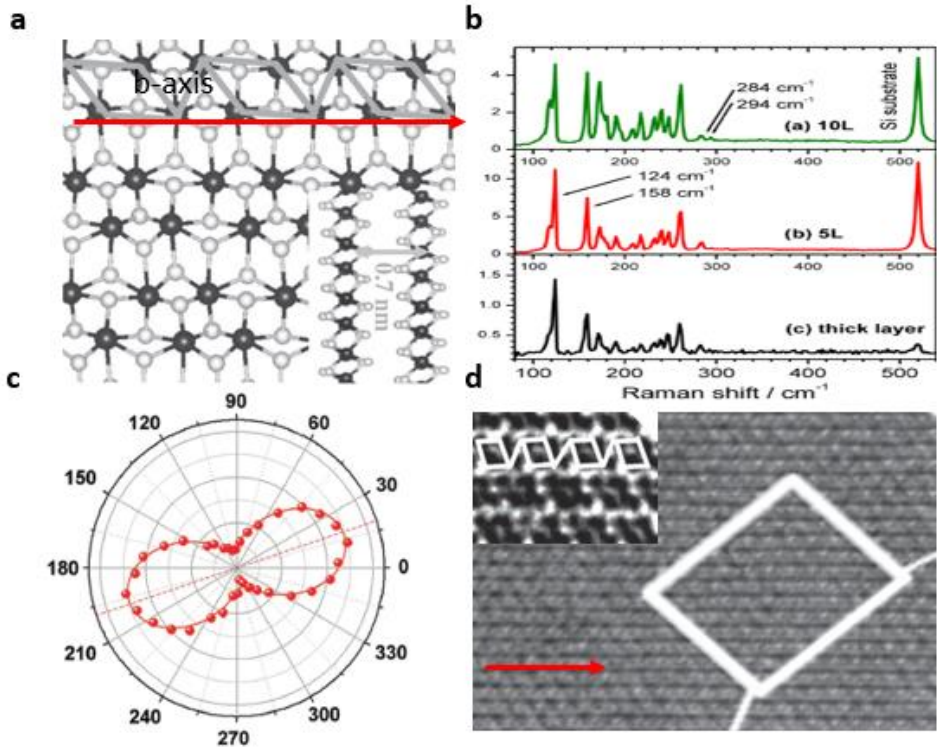

Figure 1-5 a] Top view (inset is side view) of the crystal structure of layered $ReSe_2$ simulated with the help of VESTA software, formation of Re_4 1D chains can be clearly seen [43] b] Raman scattering spectra of $ReSe_2$ on a SiO_2/Si substrate for (a) 10 layers; (b) 5 layers, and (c) a thick flake [42] c] Angle-dependent Raman intensity of ReS_2 like peak in $ReSe_2$ [44] d, Chain direction of $ReSe_2$

1.4.3 Titanium tri sulfide (TiS_3)

TiS_3 belongs to TMTCs family with monoclinic structure with theoretically calculated band gap of ~1 eV [45-48]. Crystal structure of TiS_3 can be viewed as triangular prism in MX_6 unit along the b-axis as shown in figure 1-6a. The bond length between titanium and sulfur are shorter along b-axis than a-axis [36]. This result in chain like structure leads to strong anisotropic properties. [49-50]

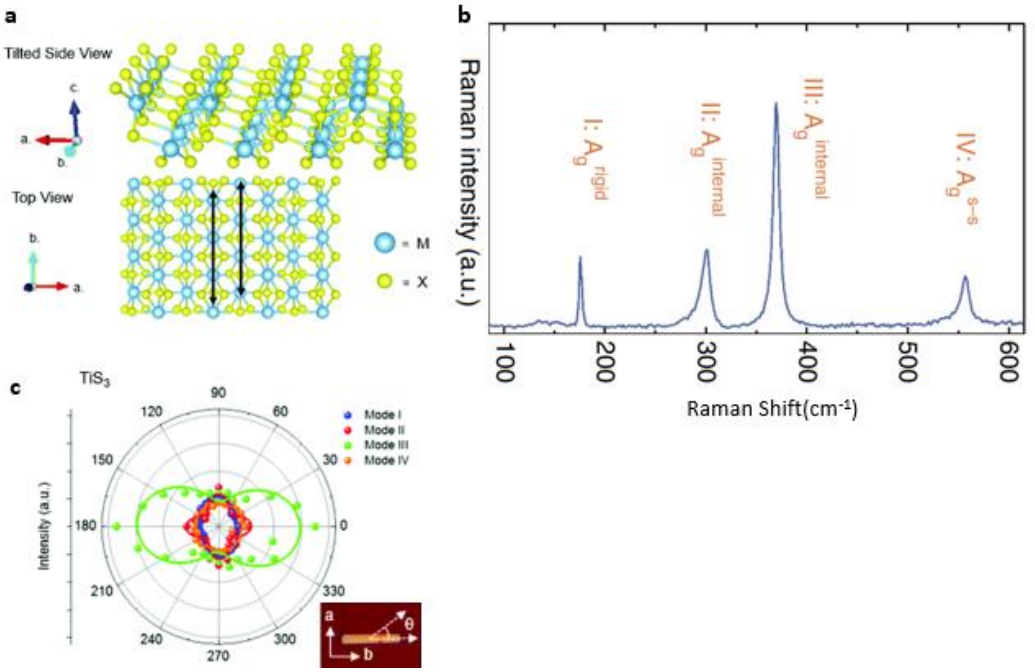

Figure 1-6 a] Tilted side view of a typical MX_3 crystal structure. A top view is shown with the black arrows indicating adjacent chain-like structures. The blue atoms represent the transition metals while the yellow atoms represent the chalcogen atoms[49] b] Raman spectrum of TiS_3 whiskers measured in ambience at room temperature [50] c] polar plot of all TiS3 modes with mode III at 372 cm^{-1} [49]

Chain direction is identified in TiS_3 using angle resolved Raman spectroscopy [49]. Raman spectrum of TiS_3 is shown in figure 1-6b. Mode I is calculated to be rigid mode between chains, mode II & III is internal chain mode and mode IV is sulfur vibration mode [50]. Generally, mode III is used to determine the chain orientation in this system since the maximum intensity of this mode is parallel to chain direction as shown in figure 1-6 c [49-50].

1.4.4 Titanium tri selenide ($TiSe_3$)

$TiSe_3$ is predicted to have the same crystal structure as TiS_3 as shown in figure 1-6a with M=Ti and X= Se. Theoretically $TiSe_3$ is an indirect band gap semiconductor with .21 eV energy and .57 eV energy in bulk and monolayer respectively. This material has not been

synthesized experimentally but possess the same anisotropic structure as TiS_3 due to having the same crystal structure. [47]

1.5 2D Alloys:

Full potential of 2D materials are limited by number of 2D materials present. Properties of current materials can be tuned further in many ways like thermal annealing, strain engineering, defect introduction and alloying. [57] Previously, conventional semiconductor alloying helped in advancement of semiconductor technology by tuning their electrical properties such as such as Si_xGe_{1-x} for high-mobility transistors, $Al_xGa_{1-x}As$ for quantum structures, $CuIn_xGa_{1-x}Se_2$ for solar cells, $In_xGa_{1-x}N$ for light emitting diodes, and $Hg_xCd_{1-x}Te$ for infrared detectors. So, alloying proved to be an effective way of tuning the interesting properties and having wide range of applications Such as catalysis, valleytronics etc. [58] Based on this experience, an early attempt was made to open or control the band gap of 1st 2D material graphene by alloying it with large band gap semiconductor h-BN [51-52]. Although this experiment failed, it led to new field in TMDCs alloy. TMDCs structure are similar with each other, having little lattice mismatch, and with varying band gap that is able to swipe band gap ranging from near IR to visible range. Researchers have demonstrated the alloys of many TMDCs such as $MoWS_2$, MoSSe, $MoWSe_2$, WSSe etc. [54-57] Also, people have performed a lot of theoretical studies to corroborate these experimental studies using DFT [53]. For instance, as shown in figure 1-7 internal energy v/s composition plot has been calculated [53]. Positive internal energy for $MoS_2/MoTe_2$ and $MoSe_2/MoTe_2$ shows that this is unfavorable as compared to internal energy of $MoS_2/MoSe_2$, which is negative in whole composition range shows its favorability. [53]

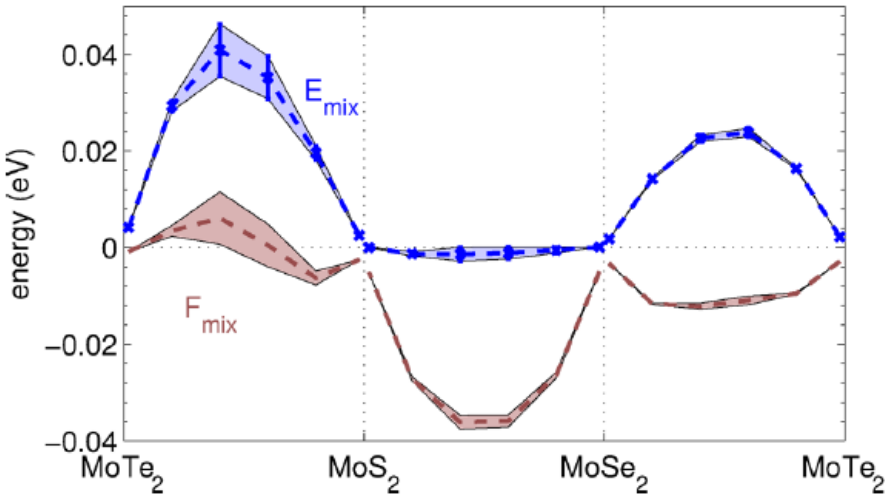

Figure 1-7 Internal E_{mix} and free F_{mix} energies of mixing per primitive cell for the $MoS_2/MoSe_2/MoTe_2$ 2D alloys. The width of the shaded areas denotes one standard deviation of the variation in calculated energies [53]

Alloying 2D materials is a very new field of study with very little prior research available for consultation. So, there is a large class of research capabilities within this field. There are also several challenges that need to be met, such as TMTCs alloys require in-depth theorization. In my work, I have alloyed anisotropic $ReS_2/ReSe_2$ and $TiS_3/TiSe_3$ and recorded their vibrational and optical properties.

Chapter 2 Synthesis and characterization

Graphene was the first 2D material synthesized from its bulk counterpart graphite. Graphene synthesis was based on a very simple technique of mechanical exfoliation. Mechanical exfoliation is performing layer by layer separation of bulk material using scotch tape. By now, researchers have found wide variety of techniques to grow these materials. Identifying the materials' structure, morphology, vibrational nature, band gap and its chemical composition is the key aspect in studying any 2D material. In this section we will develop an understanding of some of the tools used to grow and study these properties.

2.1 Top Down

Top down approach involves synthesis of bulk crystals using chemical vapor transport followed by exfoliation.

2.1.1 Chemical vapor transport (CVT)

CVT is generally used to grow high quality crystals. In this process a solid phase of materials is volatilized and transported in crystal form, generally towards the colder part from hotter part. Two main mechanisms to crystal transport are convection and diffusion. The transport agent is the primary factor in growth. Since most of the materials in 2D system are non-volatile, a volatile transport agent is required for successful transportation. Low volatility can result in no reaction and high volatility results in unstable crystal growth. Keeping that in mind, Halogen and its compounds are used as transport agents. The other key factors for growth are temperature range and the molar ratio between the metal and transport agent.

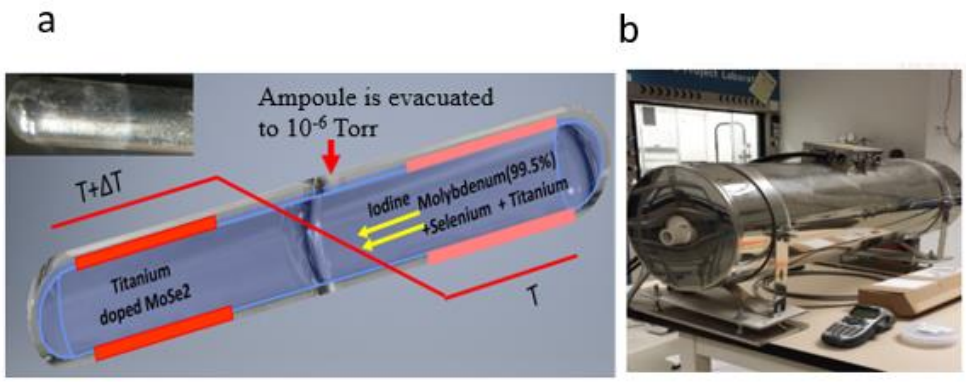

Figure 2-1 a] Typical schematic of CVT growth of crystals b] Two zone furnace used to grow all the crystals

As shown in figure 2-1 a,b, we used Thermo scientific Linderberg 3 zone tube furnace to grow our crystals. Quartz ampoule were evacuated at 10^{-6} torr and filled with elements in desired stochiometric ratio and placed in furnace at given temperature with required temperature gradient. Temperature rate was set up carefully to avoid any explosions due to exothermic reaction. The grown crystals were stored to perform further studies.

2.1.2 Micro mechanical exfoliation

As discussed earlier, first 2D material, graphene, was produced using mechanical exfoliation from its bulk form, graphite. Due to its simplicity and resulting high crystallinity, this technique has been successfully extended to other materials with weak Van der Waals force between layers.

We used silicon substrate with thermally grown 285nm silicon oxide to get better optical contrast. Silicon substrate was treated with oxygen plasma using plasma etcher to removes all the impurities from surface. Followed by this, as shown in figure 2-2, CVT grown crystals stick to the tape and peeled off layer by layer to thin it down. After that it was exfoliated

onto the cleaned silicon substrate. Exfoliated sample was viewed under optical microscope. These sample was stored in desiccator to avoid any impurity content for further characterization.

The major drawback of this technique is the limitation of size produced. Need of large area deposition has diverted the attention to other techniques such as chemical vapor deposition(CVD), atomic layer deposition(ALD) and physical vapor deposition(PVD). We will discuss CVD in the next section

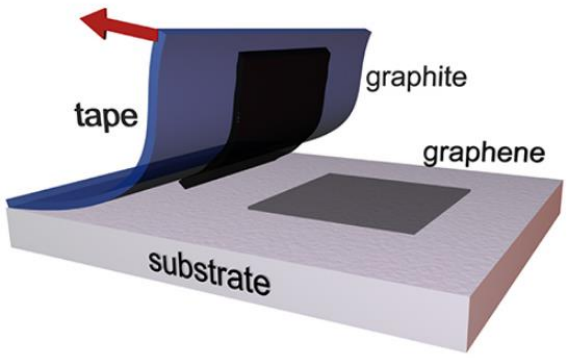

Figure 2-2 Schematic representation of the exfoliation process

2.2 Bottom Up

Foreseeing the need of 2D materials as next-gen materials, such as channel material for less than 8nm node, compelled researchers to scale up 2D materials at wafer scale. Since top down approach is only able to give us flakes at micron scale, it is not suitable for scaling up. This is why conventional semiconductors have been grown for decades at wafer scale using bottom up techniques. Bottom up techniques include Physical vapor deposition(PVD), Chemical vapor deposition(CVD) and Atomic layer deposition(ALD). 2D materials synthesis had been successfully demonstrated using each of the techniques at large scale.

2.2.1 Chemical vapor deposition (CVD)

In its simple form CVD is used to coat anything with desirable materials to enhance its properties. Precursors are introduced into the chamber generally in gaseous form with the desired substrate. Chemical reaction occurs on the hot surfaces, resulting in thin film deposition. This process is accompanied with byproducts which are evacuated out of chamber using proper abatement system. CVD is performed at varying pressure levels - ranging from millitorr to atm level, with different temperature ranges. There are many different variants of CVD available such as metal organic CVD, atmospheric CVD, organometallic vapor phase epitaxy etc. Typical atmospheric CDV schematic is shown in figure below 2-3a,b. We performed atmospheric CVD with the system shown below in our lab.

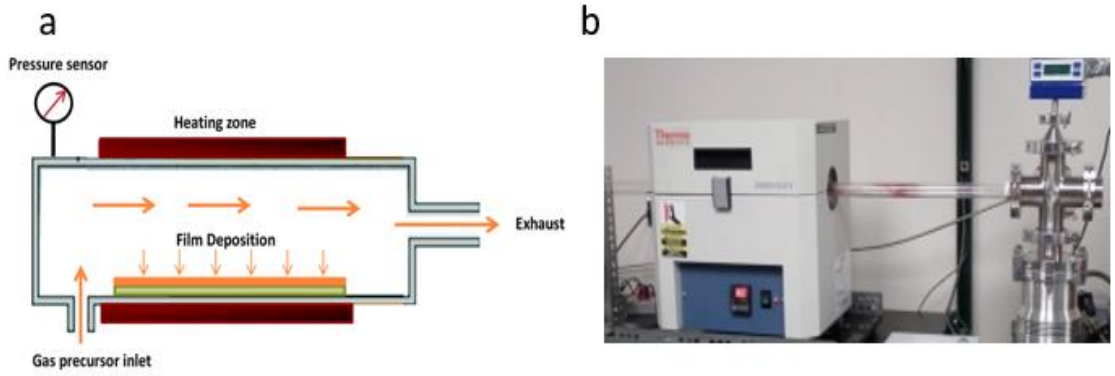

Figure 2-3 a] Typical schematic for chemical vapor deposition[59] b] CVD system used to grow 2D films

Sample preparation is the important aspect in growing these films. Effective sample preparation can charge the substrate and make it more favorable for nucleation. We used sapphire substrate to grow ReSSe alloy because of its high surface energy. Sapphire substrate was dipped in piranha solution for 10 minutes to etch out all the impurities stuck on the

surface, followed by sonication in IPA for 10 minutes. After that, the substrate was rinsed with DI water to remove all residue from the substrate followed by blowing with dry nitrogen gas.

2.3 Raman Spectroscopy

Raman spectroscopy is a nondestructive vibrational spectroscopy analytical technique used to analyze the finger print of materials. Along with finger prints, it is also used to analyze the crystallinity, thermal conductivity, defect concentration and strain of materials at microscopic level. As shown in figure 2-4, incoming monochromatic laser hits the sample and Rayleigh scattered or elastically scattered light filters out and non-elastically scattered light is detected by photo detector. Generally, non-elastically scattered light comprises of stoked and anti-stoked scattered rays. Probability of Stokes shift is more than anti stoles, Stokes shifts are used to analyze the finger print of materials.

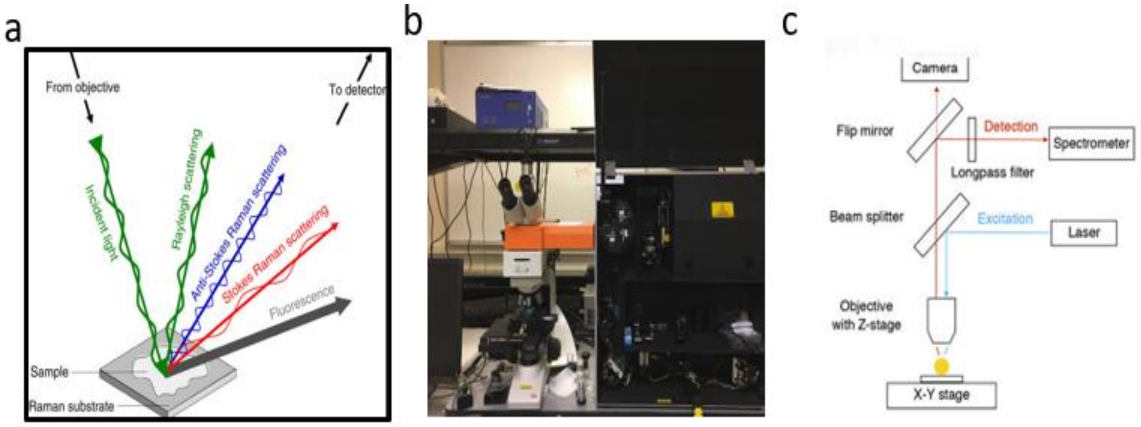

Figure 2-4 a] Schematic identifying light scattering after laser exposure on a sample surface [60] b] Raman setup used to characterize all our materials c] Typical Raman setup schematic

As shown in figure 2-4c typical Raman is consists of four major components:

i. Laser excitation source

ii. Optics/Camera

iii. Wavelength filter

iv. Laser detector/Spectrometer

Since majority of back scattered light is filtered out, and rest of the Stokes and anti-stokes signal constitute a very small percentage, careful measurement needs to be performed to enhance signal to noise ratio. Measurement should be performed at low laser power to avoid sample burning and with high number of accumulation over a larger scan period to increase signal to noise ratio.

2.4 Angle Dependent Raman Spectroscopy

Chain direction in quasi-1D systems can be identified using angle resolve Raman spectroscopy. Normal and orthogonal polarization is offered by our setup. As shown in figure 2-5 a, b, in normal setup, incident and detected light is parallel to each other; and in orthogonal setup incident and detected light is perpendicular to each other.

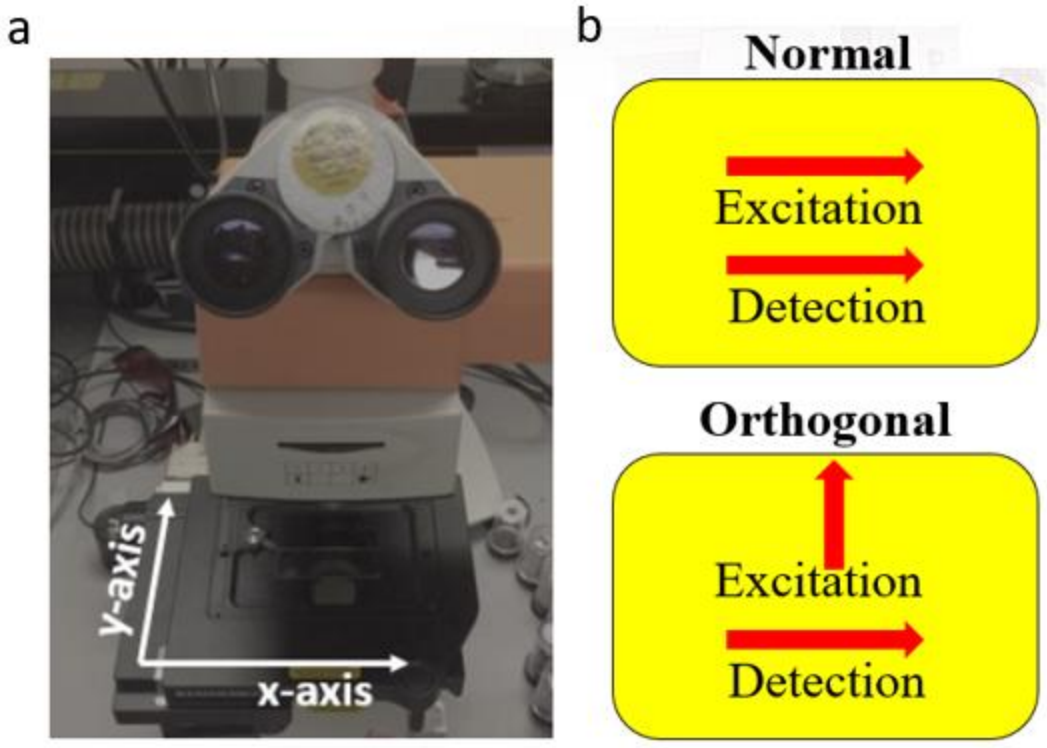

Figure 2-5 a] Rotating stage under optical microscope for angle-resolved Raman measurement b] Normal and orthogonal arrangements to perform angle dependent measurements

We used normal setup to study the $ReS_{2x}Se_{2(1-x)}$, $TiS_{3(1-x)}Se_{3x}$. Sample was placed on rotating stage and flakes were located using 100X magnification under microscope. Sample was oriented at zero-degree w.r.t polarization direction and then rotated till 360 degrees with steps of 15 degrees. Raman spectrum was located at the same spot for all the angles. Data interpretation was done using polar plot of intensity v/s angle for all the Raman active peaks. Polar plots obtained are generally two lobed, three lobed or four lobed. Two lobed peaks are used to indicate the chain direction or anisotropy direction.

2.5 Photoluminescence (PL)

Raman spectroscopy and photoluminescence can be performed on same equipment. This technique depends on creation of electron hole pairs followed by their radiative recombination. In this technique electrons are excited from valence band to conduction band with light of energy greater than materials band gap. The resulting photon due to recombination as shown in figure 2-6b is measured using the detector. These emitted photon helps in extracting out various optical properties and defect concentration of materials. As shown in figure 2-6a, there are four types of recombination - band to band recombination, free exciton recombination at donor or acceptor level, and bound excitonic recombination.

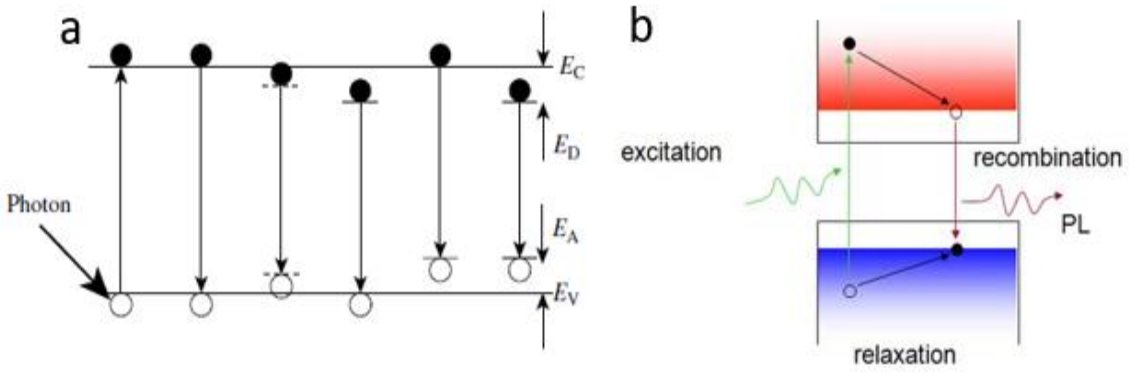

Figure 2-6 a] Different types of recombination's in materials b] Typical photoluminescence schematic

This technique is only efficient with direct band gap materials in which the conduction band is just below the valence band with no momentum change. In indirect band gap, electron excitation is accompanied by phonon due to momentum change and that leads to non-radiative recombination.

We can easily extract the optical band gap of direct band gap materials with the spectra obtained by this technique. We obtained intensity v/s energy graph using this; and energy value at the peak intensity position is the band gap of material. We can also compare the quality of the sample by comparing it with spectrum of defect free materials.

2.6 Atomic force microscopy (AFM)

AFM is a unique tool to analyze the surface science of any material. AFM setup, shown in figure 2-7a, consists of a cantilever with a sharp tip mounted on its end. For imaging, the tip is brought into continuous contact in contact mode or intermittent contact in tapping mode with the sample and scanned across the sample surface. In our system piezoelectric scanners translate cantilever over the sample. The motion of the cantilever is sensed by light reflected from the cantilever. The cantilever motion causes the reflected light to impinge on photodiode. Holding the signal constant, by varying the sample height through a feedback arrangement, gives the sample height variation. Figure 2-7b shows height profile of compact disk using this technique. AFM operates in several modes such as contact mode, non-contact mode and tapping mode.

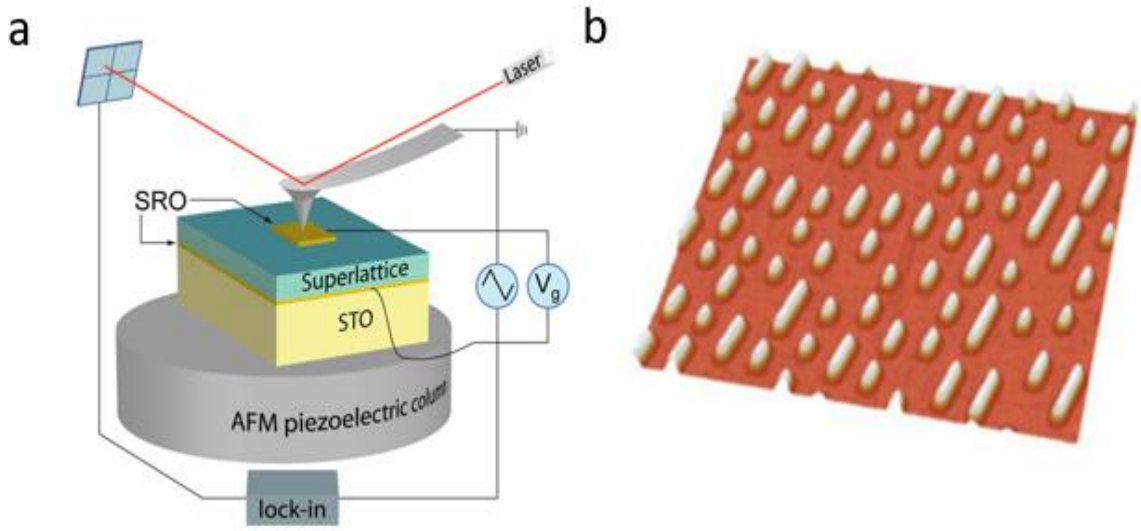

Figure 2-7 a] Setup for AFM measurement of piezoelectric properties of thin films using a metallic electrode on the film surface b] AFM Image of CD drive

AFM is very sensitive to small dirt particles adhering to sample. Sample cleaning is thus the most important step before performing measurements. Since all the materials measured were very stable in water, sample was cleaned by rinsing in DI water and blown with nitrogen. After cleaning, sample was transferred onto a metallic disc to mount sample for piezoelectric stage. Image was taken under tapping mode to avoid any rubbing with sample, using standard tip. Next, the gains were controlled, samples per line was set at 386 to get high resolution AFM images.

2.7 X-Ray Diffraction (XRD)

As shown in figure 2-8a, XRD is used to analyze crystallinity, phase identification, quantitative analysis, lattice parameters and crystallite size. In very simplifies system X-ray incident on to the surface of the crystal for range of angles (2 theta). All these diffracted waves have constructive and destructive interference. A detector plots the constructive

interference v/s angle. Using these theta values corresponds to constructive interference, we can extract out all the information. As shown in figure 2-8b this technique is based on Bragg's law. Constructive interference only happens for x-ray diffracted from two planes. Using this we can easily extract out the d spacing of our materials.

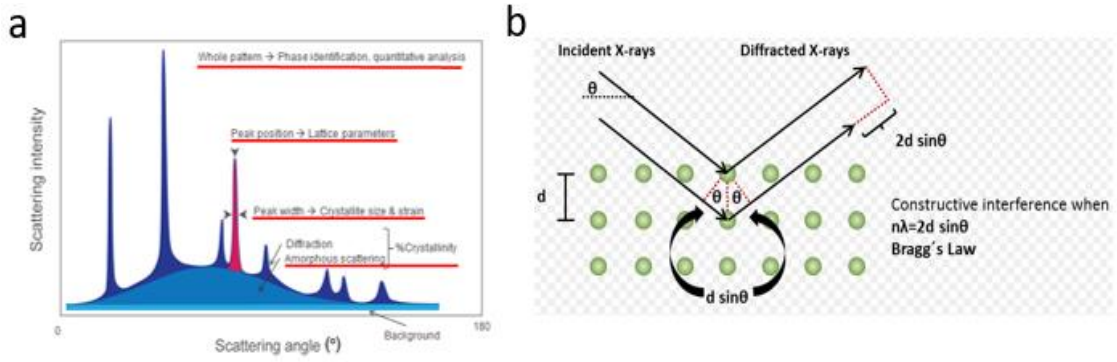

Figure 2-8a] Typical XRD spectrum showing information that can be extracted out b] XRD working principal

The XRD patterns were recorded on ReSSe and TiSSe alloys on Siemens D5000 x-ray diffractometer machine using Cu Kα radiation with wavelength = 1.54 A. Crystal was made flat and places on zero background plate and XRD pattern was recorded with scan rate of 5 degree per minute from 15 degrees to 60 degrees.

2.8 Energy Dispersive Spectrometers (EDS)

EDS is commonly using to quantify the element present in your sample. It is generally employed on TEM or SEM and uses electron beam, deflection coils and focusing lens. Its fundamental principal is based on each element having a unique atomic structure allowing the creation of a set of peaks on its electromagnetic emission spectrum. In this setup, X-ray is emitted to the sample which ejects the electron from an atom in ground state, creating a hole. This hole is filled by electron in higher state that then emits x-rays. Energy of the

emitted x-ray is measured by EDS which is characteristic to element present in the material. We used EDS in SEM to measure our samples. ReSSe and $TiS_{2.76}Se_{.24}$ was exfoliated on carbon tape and placed under high magnification and scanned. This gives us intensity v/s energy spectra. These energy value can be matched with available database and elements can be identified.

Chapter 3 Alloy of 1T' phase of TMDC ($ReS_{2x}Se_{2(1-x)}$)

3.1 Introduction

Alloying 2D materials provides us flexibility to tune optical, electrical and mechanical properties of materials such as band gap, carrier type, thermal conductivity, electrical conductivity, mobility etc. Until now, many 2H phase of TMDC alloy have been successfully demonstrated like $MoS_{2(1-x)}Se_{2x}$, $Mo_{1-X}W_xS_2$, $WS_{2(1-x)}Se_{2x}$ etc. In this work we have alloyed ReS_2 and $ReSe_2$ which are 1T' phase of TMDCs that also exhibit anisotropy. As mentioned earlier, ReS_2 has the band gap of 1.6 eV and $ReSe_2$ has band gap of 1.27 eV. By alloying them we can vary the band gap in this range which can be very useful for many applications.

In this work we have addressed the fundamental question of whether we can even alloy these two materials. We have also studied its vibrational nature & optical band gap and how they differ from its parent compounds. Peaks contributing to anisotropic chain direction have also been identified. We demonstrated large scale synthesis of these alloys using CVD and compared its vibrational properties, anisotropic ratio etcetera with the CVT grown crystals.

3.2 Crystal Structure

Isostructural nature of ReS_2 and $ReSe_2$ results in the same crystal structure for ReSSe which is confirmed by XRD data and TEM images. As shown in figure 1-4a, it crystallizes in distorted 1T phase, in which Re atom is sandwiched between sulfur and selenium layers; blue corresponds to Re atom and yellow corresponds to sulfur and selenium atoms. As explained

in chapter 1, presence of extra electron in Re atom results in dimerization and this forms diamond chain-like structure between Re atoms as shown in figure 3-1.

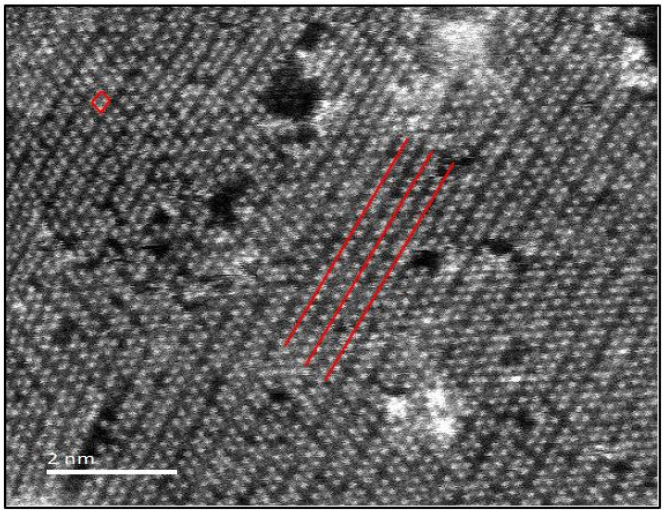

Figure 3-1 High resolution TEM showing diamond like chain structure of ReSSe

3.3 Chemical vapor transport (CVT)

ReSSe crystal was grown using approximately same method used by Huang et.al [61]. Figure 3-2b shows the typical setup for this growth. This method consisted of two steps, first amorphous powder was prepared using Re (99.9%), S (99.98%) and selenium (99.98%) mixed in stoichiometric ratio and placed in evacuated ampoule at 1030°C for 5 days. After that 5g of sample was introduced into the ampoule evacuated at 10^{-6} torr for 10 days at 1050°C, with temperature gradient of 100°C, and with I_2 as transport agent. The inner diameter of the tube being 15 mm and the length 210 mm. Care was taken in ramping up the temperature due to possibility of an explosion due to exothermic reactions inside the ampoule. Crystals obtained from this growth have a silver color with sheet-like appearance

as shown in figure. ReSSe flakes were exfoliated into few layers, as shown in figure 3-2, on Si/SiO_2 substrate from the wall of the ampule.

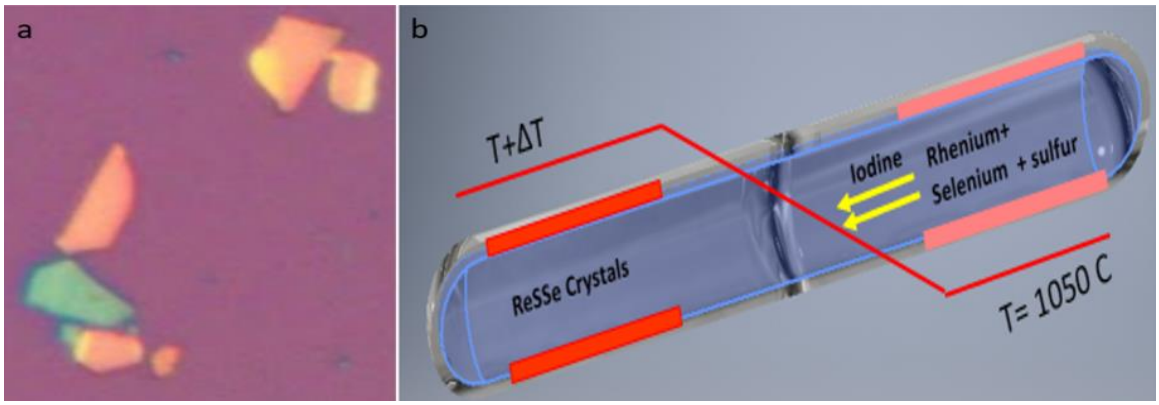

Figure 3-2 a] Optical image of exfoliated ReSSe crystal on Si/SiO_2 substrate b] Typical schematic of CVT growth of ReSSe crystals

3.4 Chemical Vapor Deposition (CVD)

This was the first time we have demonstrated the possibility of large scale growth of ReSSe alloys using this technique. Figure 3-3 shows the setup used to grow these materials using this technique. Prior to growth, sapphire substrates were treated with oxygen plasma for 3 minutes to remove any contaminants on the surface and placed inside a small glass tube containing ammonium perrhenate (NH_4ReO_4 Sigma-Aldrich, ≥99%) precursor. This tube was placed at the center of the heating zone of the furnace, and sulfur and selenium (≥99.98% Sigma-Aldrich) precursor was placed approximately 18.5 cm upstream from the NH_4ReO_4 precursor. The growth was performed at atmospheric pressure (atm), and precursors were transported to the substrate under high purity argon and hydrogen flow. Samples were first heated to 300°C (100 sccm AR flow), and flow was gradually decreased to

50 sccm at growth temperature (490−520°C). Sulfur and selenium precursors were sublimated at ~350−420°C temperature range and carried to the surface by AR flow. Growth was carried out at 490−520°C for 25 minutes followed by controlled cooling (5°C min−1) to 420 °C and fast cooling (>10°C min−1) to room temperature. Flake obtained from this varies in morphology depending on growth temperature as shown in figure 3-3. These sample were stored under vacuum for further characterization.

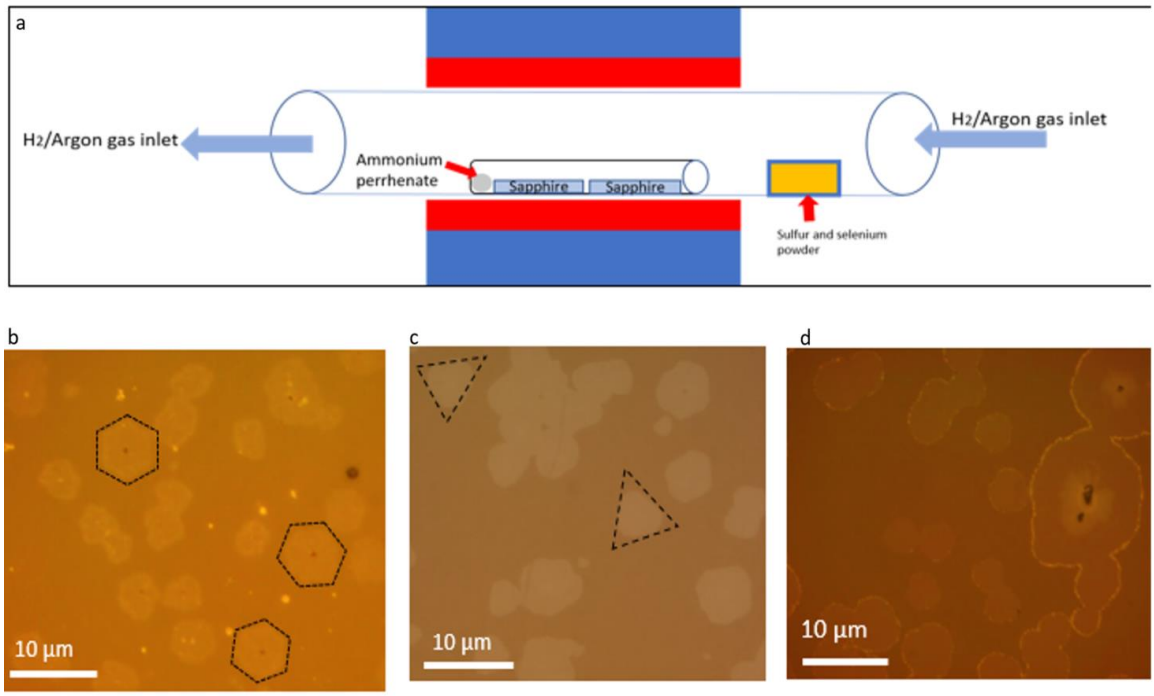

Figure 3-3 a] Schematic of CVD growth of ReSSe crystals b,c,d Different morphology of ReSSe film grown by CVD at different temperature

3.5 Atomic Force Microscopy

Brooker Dimension Multimode 8 tool setup, under tapping mode, was used to measure the height profile of alloy of these materials. The resolution was set at 256 x 256,

and scanning rate was 512 points per line. Height profile of both exfoliated and CVD grown samples were measured. As shown in figure 3-4 below, thickness obtained from exfoliated sample measured out to be 1.5nm, which is approximately a bi-layer. Thickness was ~.7nm for CVD grown flakes, which was the same as previous monolayer growth reported for CVD ReS_2 and $ReSe_2$. Also from figure 3-4b we can see that dendritic nature of CVD grown hexagonal flakes may be one of the reasons for loss in anisotropy, which will be discussed in the next sections.

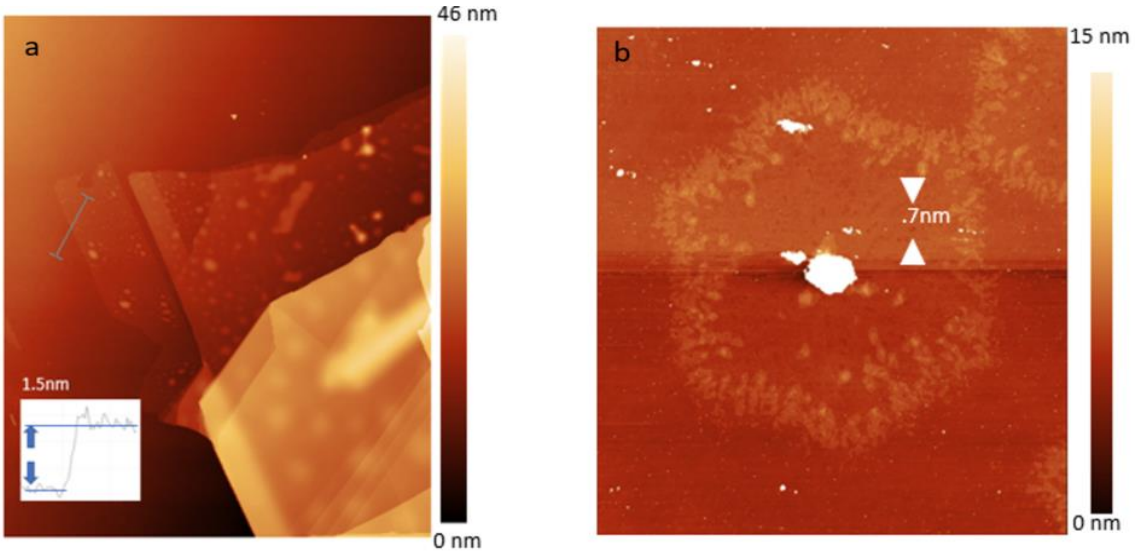

Figure 3-4 a] AFM image shown bilayers of exfoliated ReSSe flake b] AFM image showing monolayer of ReSSe film grown using CVD

3.6 X-Ray diffraction (XRD)

Setup mentioned in section 2.7 was used to collect XRD data on our crystal. For measurements, a flat piece of crystal was mounted onto zero background plate, and 2 theta angles ranging from 5 to 65 degrees was scanned. Figure 3-5 shows XRD spectrum of all

three crystals. Sharp XRD peaks show highly crystalline nature of materials. Also, it is easily inferred from the XRD data that increase in sulfur content in $ReSe_2$ will decrease the d-spacing of material because of smaller size of sulfur atom as compared to selenium. Hence theta will shift to higher value.

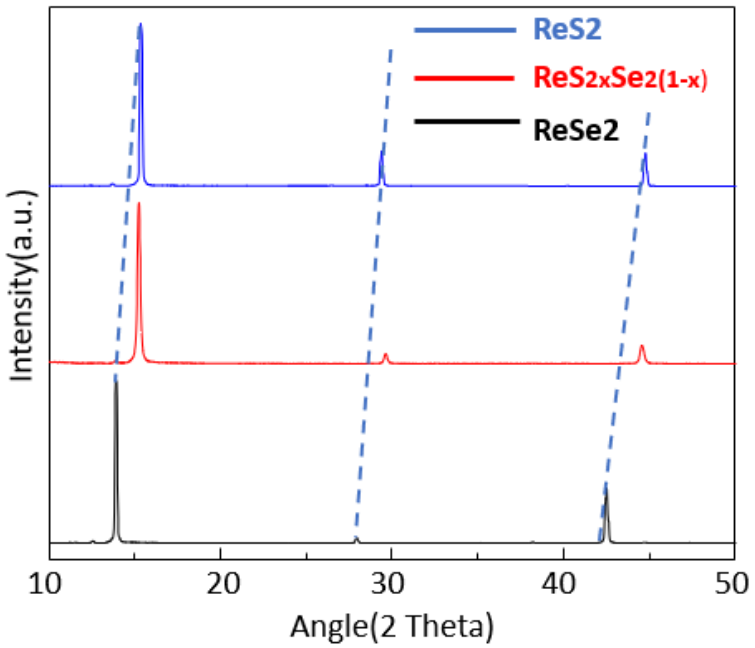

Figure 3-5 XRD spectrum of ReSSe crystal and its comparison with ReS_2 and $ReSe_2$

3.7 Energy dispersive X-ray Spectroscopy (EDX)

Qualitative Elemental analysis was performed on CVT grown crystal using EDX. Figure3.6 shows the presence of Rhenium, Sulfur and selenium confirm the alloying behavior of ReSSe. From the compositional analysis sulfur to selenium ratio comes out to be in ratio of one is to one. Extra copper peaks in the figure is because of sample was transferred onto

copper grid for measurement. Since CVD samples were very thin it was hard to do EDX on those samples.

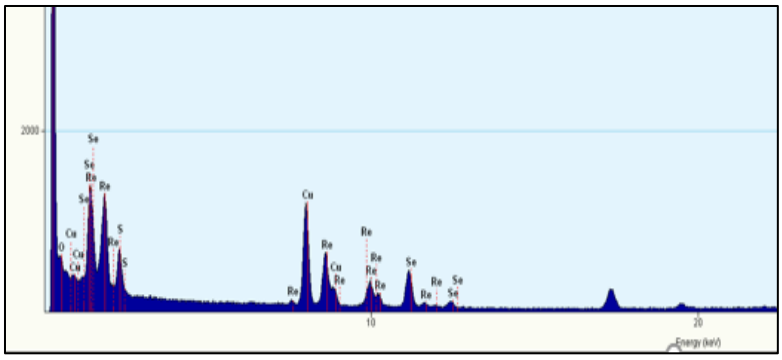

Figure 3-6 EDX spectrum showing presence of rhenium, selenium and sulfur atoms in exfoliated ReSSe flakes

3.8 Photoluminescence (PL)

As defined in chapter 1, optical band gap of ReS_2 and $ReSe_2$ is 1.57 eV and 1.26 eV respectively. Optical band gap of alloy was measured using the same setup as described in section 2.8 at room temperature. Figure 3-7 shows the PL emission for our alloy is 1.39 eV, which lies between band gap of $ReSe_2$ and ReS_2. Full range of band gap tuning as a function of different alloy compositions is also reported by Wen et al [44].

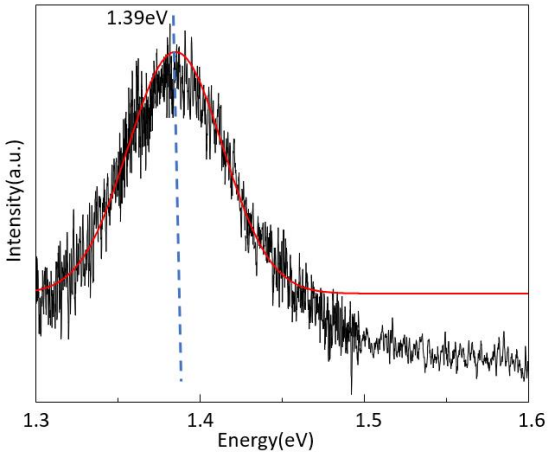

Figure 3-7 Band gap of CVT grown ReSSe crystal using photoluminescence spectroscopy

3.8.1 Temperature and power dependent PL

Temperature dependent PL measurement was also carried out under vacuum, by heating and cooling the sample in a microscope cryostat with temperature controlled between 77K and 300K. Figure 3-8b shows the PL v/s Temperature graph for ReSSe alloy; all the data points show the same trend of increasing band gap with decreasing temperature and nonlinear behavior at low temperatures as observed for $ReSe_2$ and ReS_2. This phenomenon can be explained by Varshnis phenomenon [62]. Varshni theorizes the two possible explanations for this to happen. One, this change in band gap can happen due to temperature dependent dilation of lattice. This effect is linear at higher temperature and nonlinear at low temperature. Two, the major contribution of shift comes from electron lattice interaction.

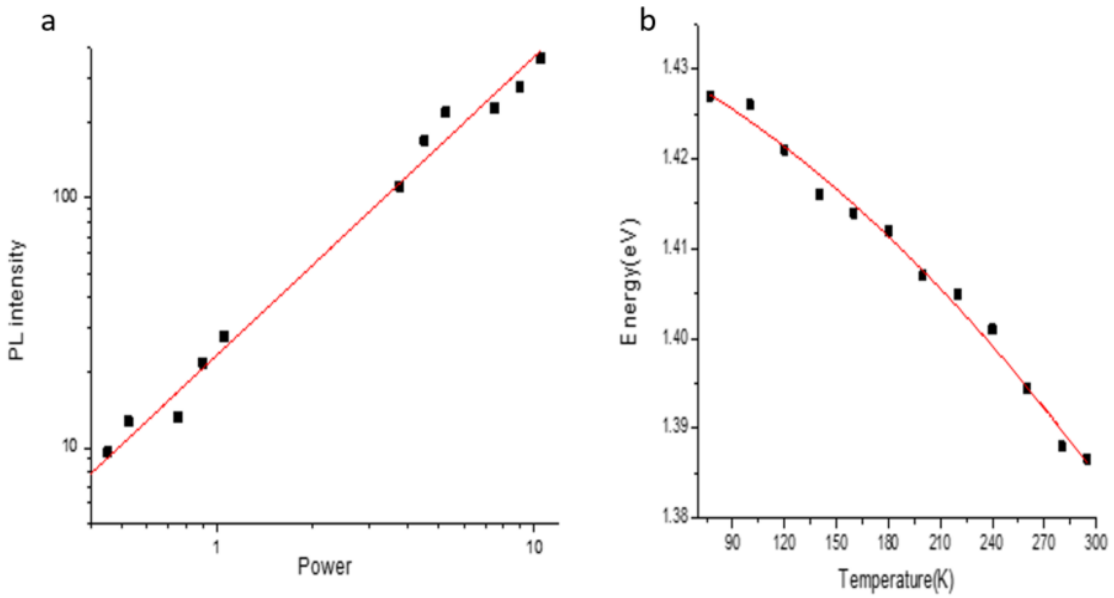

Figure 3-8 a] Plot of PL intensity v/s Power for ReSSe b] Temperature dependent PL for ReSSe crystal from 77K to 300K

The photoluminescence of ReSSe was also measure with varying laser power. The excitation power ranges from .075mW to 7.5mW. The sample was mounted on same cryostat discussed above and measurement was performed at 77K to avoid burning of sample at high laser power. Slope of ~1 for PL intensity v/s laser power suggest that it is a monomolecular process that corresponds to exitonic recombination.

3.9 Raman Spectroscopy

Theoretically 18 Raman active vibrational modes can be observed for both ReS_2 and $ReSe_2$ [42,63]. Typical Raman spectra for ReSSe alloy is shown in figure 3-9, and its comparison with ReS_2 and $ReSe_2$. For ReS_2, vibration modes are in range of 100-450 cm^{-1} and $ReSe_2$ they

are in range of 100 to 300 cm^{-1}. As shown in figure 3-9 above, Raman frequency for all mode blue shifts with increase in sulfur content attributed to lower mass of sulfur atoms in comparison to selenium. As per the literature, low frequency peaks are attributed to Re-Re vibration. ReS_2 has very few peaks in 100 cm^{-1} to 300 cm^{-1} as compared to $ReSe_2$, peaks in this range are attributed to Se-Se vibration. Also, $ReSe_2$ has no peaks above 300 cm^{-1}, so all the modes shown in figure 3-9 after 300 cm^{-1} in ReSSe is corresponds to sulfur atom vibrations. From analysis we anticipated 196 cm^{-1} as phonon mode V, which corresponds to 172 cm^{-1} in $ReSe_2$ and 211 cm^{-1} in ReS_2. This peak is the characteristic mode for identifying Re-Re chain direction in both materials.

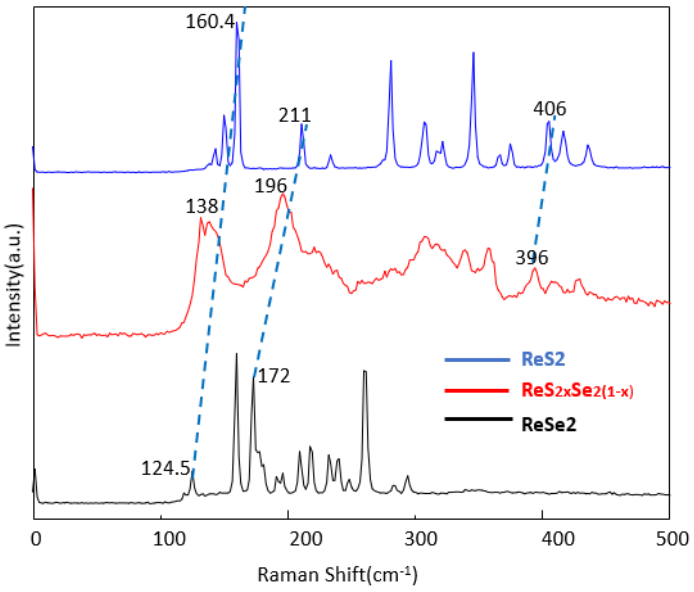

Figure 3-9 Raman spectrum of exfoliated ReSSe flakes and its comparison with ReS_2 and $ReSe_2$ Raman spectrum

We also performed anisotropic measurements to find out characteristic peaks to identify chain direction, which we will discuss in next section.

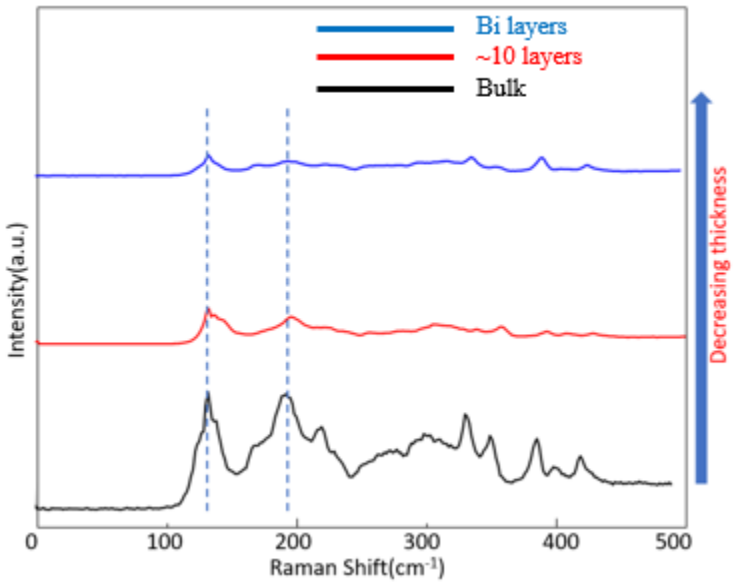

Figure 3-10 Thickness dependent Raman spectrum of ReSSe

As discussed in chapter one, ReS_2 and $ReSe_2$ are electronically and vibrationally decoupled due to Peierls distortion of 1T structure which prevents ordered stacking and minimizes the interlayer overlap of wave functions. Owing to isostructural nature of ReSSe, we also studied this in our alloy by observing Raman modes with varying thickness. There is no major shift in Raman spectrum as shown in figure 3-10, except the reduction in intensity with decrease in thickness.

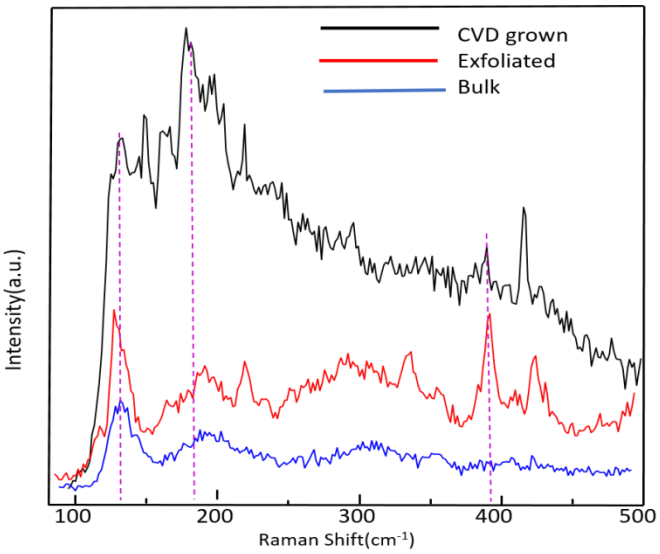

Figure 3-11 Raman spectrum of CVD grown ReSSe alloy and its comparison with the CVT grown ReSSe

Figure 3-11 shows Raman spectrum of CVD grown sample and its comparison with exfoliated samples. Approximately similar vibrational modes have been observed in CVD grown samples, except that they display very large backgrounds. Large background in CVD grown sample is attributed to larger number of defects as compare to CVT grown sample.

3.10 Angle Resolved Raman Spectroscopy

The previous setup explained in chapter 2 has been used to measure anisotropy of CVT and CVD grown ReSSe. We took our measurements in the normal configuration, where incident light is parallel to detection. All the measurements were taken in an interval of 15 degree at the same spot with very little laser power to avoid sample burning. The main aim of this study was to identify characteristic peak to identify chain direction in the alloy.

3.10.1 Exfoliated flakes

Since this material is vibrationally and electronically decoupled, we chose a relatively thick sample. Polarization dependent Raman spectra were collected by using a 488 nm linearly polarized laser incident on the sample in z direction. We used the Re-Re atom vibration mode of 196cm^{-1}, corresponding to 212 cm^{-1} ReS_2 peak and 172 cm^{-1} ReSe2 peak, to identify the chain direction. To demonstrate the variation, Raman intensity of 196cm^{-1} has been shown in figure 3-12. Polar plot shows the two-lobed symmetry with maximum intensity of 196cm^{-1} peak occurs at 0 and 180 degree and minimum intensity occurs at 90 and 270 degrees.

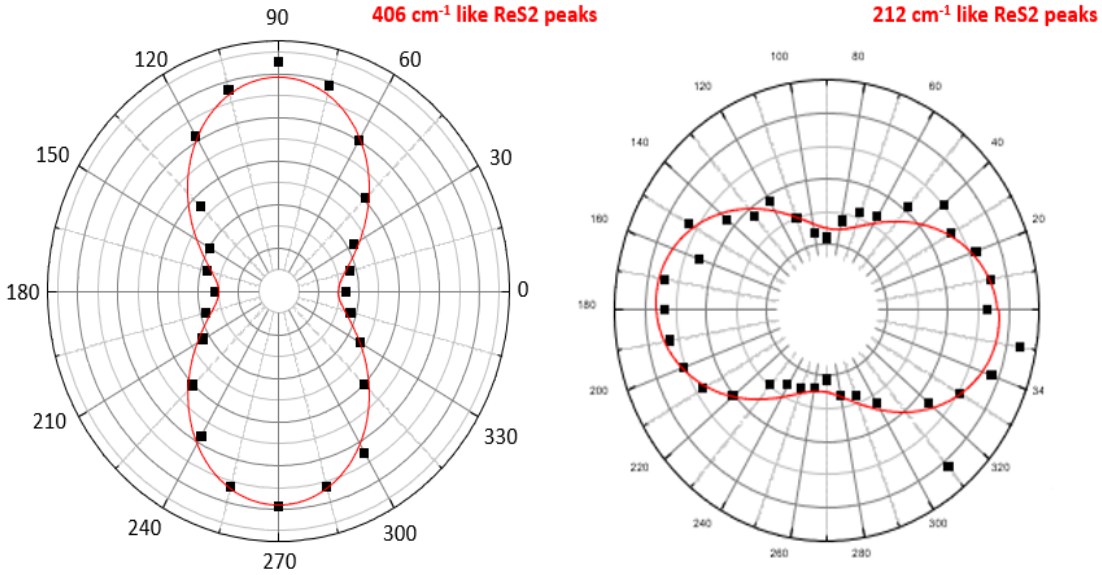

Figure 3-12 Polar plot of 406 cm^{-1} and 212 cm^{-1} like ReS2 peaks of ReSSe

3.10.2 CVD grown samples

The previous setup has been used for CVD, for polarization measurement. We chose a thin hexagonal like ReSSe flake for our measurement and took measurement on all six domains. To demonstrate the intensity variation Raman intensity of 196 cm^{-1} has been shown in figure below. All the domain shows two lobed polar plots with maximum intensity always perpendicular to edge of hexagon. This finite anisotropy behavior is similar to CVD ReS_2 reported by Kedi et al [50].

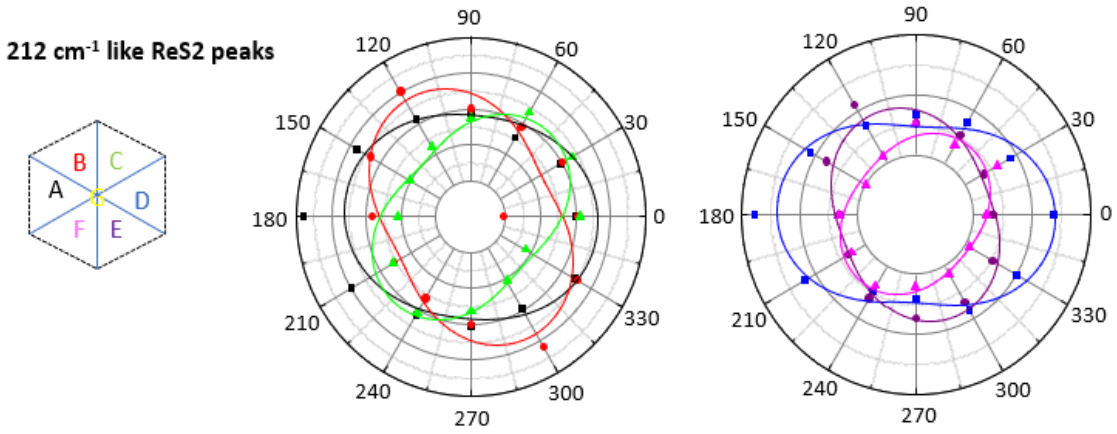

Figure 3-13 Angle-dependent polar plots of CVD flake for domain - A (black), B (red), and C (green), D (blue), E (purple), and F (pink) in a hexagonal flake.

3.11 Anisotropic Ratio Comparison Between CVD And Exfoliated Flakes

Anisotropic ratio is calculated by dividing maximum intensity to minimum intensity. As shown previously, dendritic growth in AFM image signal the loss of anisotropy. To analyze the loss of anisotropy we collected polarization data on ~ 10 different samples of CVD and CVT grown samples, and plotted the most prominent Re-Re chain vibration peak

196 cm^{-1}, as shown in figure 3-14a. The box plot with ~10 data points showing the anisotropy ratio is always higher in CVT grown sample as compared to CVD grown sample.

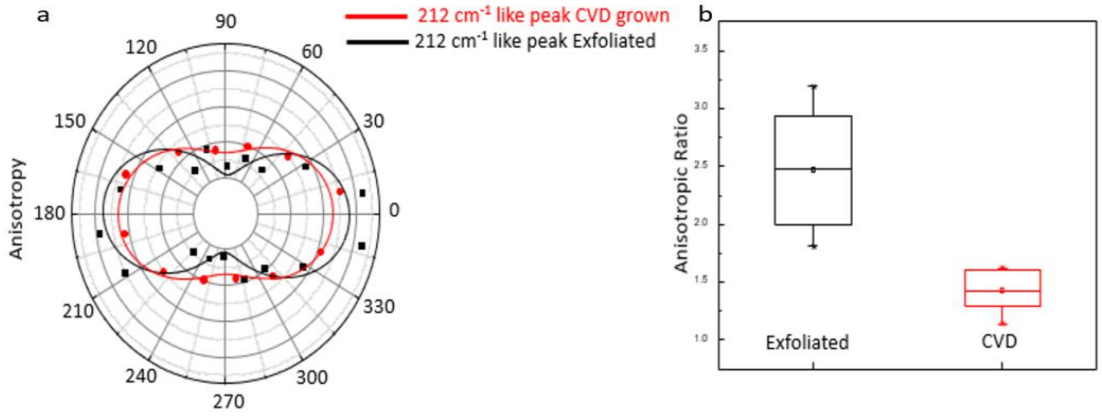

Figure 3-14 a] Polar plots showing comparison of anisotropy in exfoliated v/s CVD grown samples b] Box plot of anisotropic ratio comparison between exfoliated and CVD grown sample

3.12 Loss of Anisotropy in CVD Grown Samples

As stated in the previous section, there is a loss of anisotropy in the CVD grown sample. We performed a detailed analysis of CVD grown sample using TEM images. Different orientations of chain direction and amorphous growth in CVD grown sample contributed to loss of anisotropy. As shown in figures 3-15, different colors are attributed to different chain direction, while pink color is attributed to the amorphous region. Different chain direction results in loss of overall anisotropy.

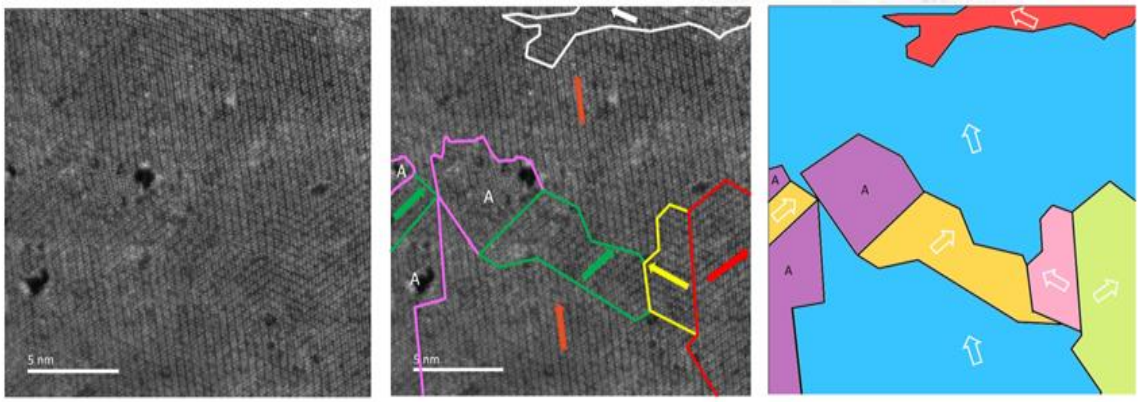

Figure 3-15 High resolution TEM images showing grain boundaries, different domains and amorphous region

Although we were successful in growing large scale $ReS_{2(1-x)}Se_{2x}$ alloy, but owing to large number of defects and grain boundaries as detailed above, this material may not be suitable for device application at an industrial scale. Thus, we need to work on controlled anisotropic growth with minimal defects and large range order. We did some preliminary work on controlling the anisotropy of CVD grown sample, which will be discussed in the future work.

Chapter 4 Alloy of MX_3- $TiS_{3(1-X)}Se_{3X}$

4.1 Introduction

Until now only one alloy from TMTCs, $Nb_{1-x}Ti_xS_3$, has been successfully demonstrated. In this work we alloyed TiS_3 and $TiSe_3$ both of which have monoclinic structure and exhibit anisotropy. As mentioned earlier, theoretical band gap of monolayer TiS_3 is ~1.0 eV and monolayer $TiSe_3$ has band gap of .54 eV. Alloying them can be very useful for various IR application.

In this work we have answered the very basic question, whether we can alloy these two materials and what percentage of selenium can be alloyed by theoretical calculation. We have also studied its vibrational nature and studied how it is different from its parent compounds. Peaks contributing to anisotropic chain direction have also been identified.

4.2 Crystal Structure

Isostructural nature of TiS_3 and $TiSe_3$ results in the same crystal structure for $TiS_{2.76}Se_{.24}$ crystal has been confirmed by our diffraction pattern imaging using TEM as shown in figure 4-1c. Chain direction is shown in figure 4-1a. It crystallizes in monoclinic phase, with pseudo 1D like structure.

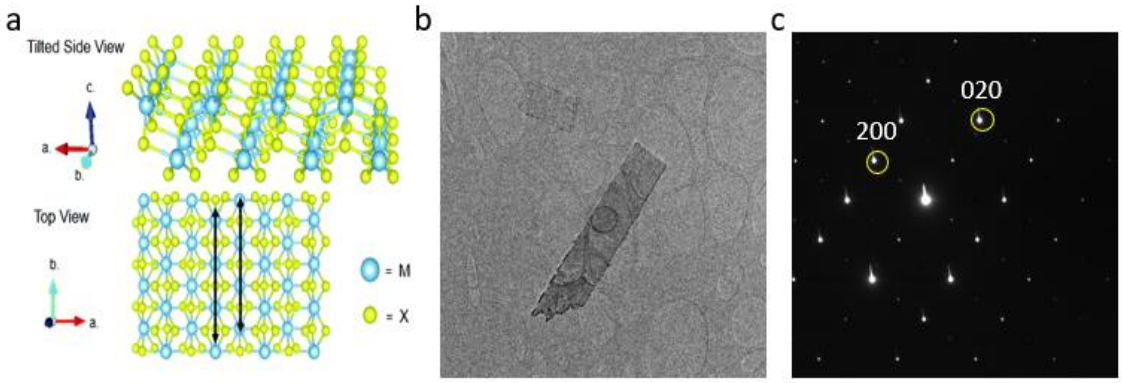

Figure 4-1 a] Side view and Top view of monoclinic structure of TiS_3 b] Flake of $TiS_{2.76}Se_{.24}$ on TEM grid c] Diffraction pattern of $TiS_{2.76}Se_{.24}$ showing 200 and 020 directions.

4.3 Chemical Vapor Transport (CVT)

This was the first time when $TiS_{2.76}Se_{.24}$ crystal was grown using CVT method. Figure 4-2c shows the typical setup for this growth. This method consisted of two major steps, first mixture was prepared using titanium sheets, sulfur (99.98%) and selenium (99.98%) mixed in stoichiometric ratio. After that, 2g of sample was introduced into the ampoule evacuated at 10^{-6} torr for 7 days at 550°C with temperature gradient of 100°C with I_2 as transport agent. The inner diameter of the tube being 15 mm and the length 210 mm. Care was taken in ramping up the temperature due to possibility of an explosion due to exothermic reactions inside the ampoule. Crystals obtained from this growth have a silver color with needle like appearance as shown in figure 4-2a,d. $TiS_{2.76}Se_{.24}$ flakes were exfoliated into a few layers as shown in figure 4-2c on Si/SiO_2 substrate from the wall of the ampoule. Wide range of growth parameters were tested by varying the temperature from 450 ºC to 650 ºC and amount of selenium from 20% to 80%. At 20% selenium and temperature around 550 ºC,

results obtained are shown in the above grown composition. Temperature greater than 590 ^{o}C results in TiS_2-like crystals with similar sulfur to selenium stoichiometric yield as loaded in the ampoule. This suggested that more than 8% selenium in immiscible in TiS_3.

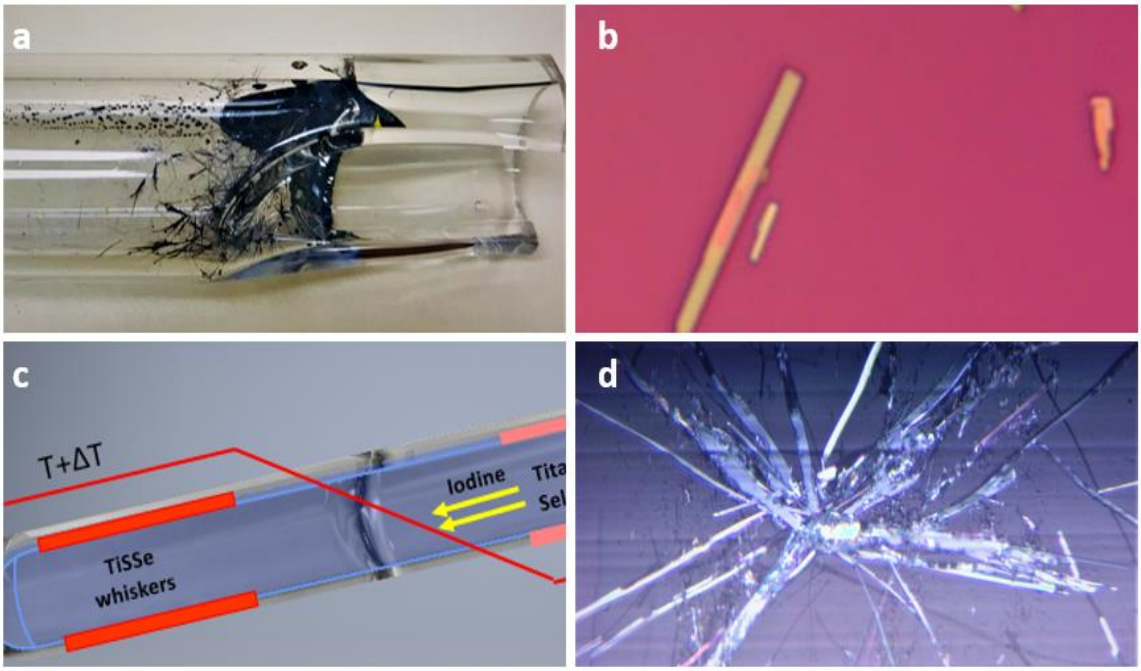

Figure 4-2 a] Ampoule showing $TiS_{2.76}Se_{.24}$ growth b] Optical image of exfoliated $TiS_{2.76}Se_{.24}$ nanowire on Si/SiO_2 substrate. C] Typical CVT growth setup of $TiS_{2.76}Se_{.24}$ d, $TiS_{2.76}Se_{.24}$ Nano wire like crystals after CVT growth

4.4 X-Ray Diffraction (XRD)

The previous setup was used to collect XRD data for our crystal. For measurements, a flat piece of crystal was mounted onto zero background plate and 2theta angle ranging from 5 to 65 degrees was scanned. Figure 4-3 shows XRD spectrum of all three crystals. Sharp XRD peaks indicate highly crystalline nature of materials. Also, it is easily inferred from the XRD data that increase in Selenium content in TiS_3 will increase the d-spacing of

material due of larger size of selenium atom as compared to sulfur. Hence theta will shift to lower value as compared to pure TiS_3.

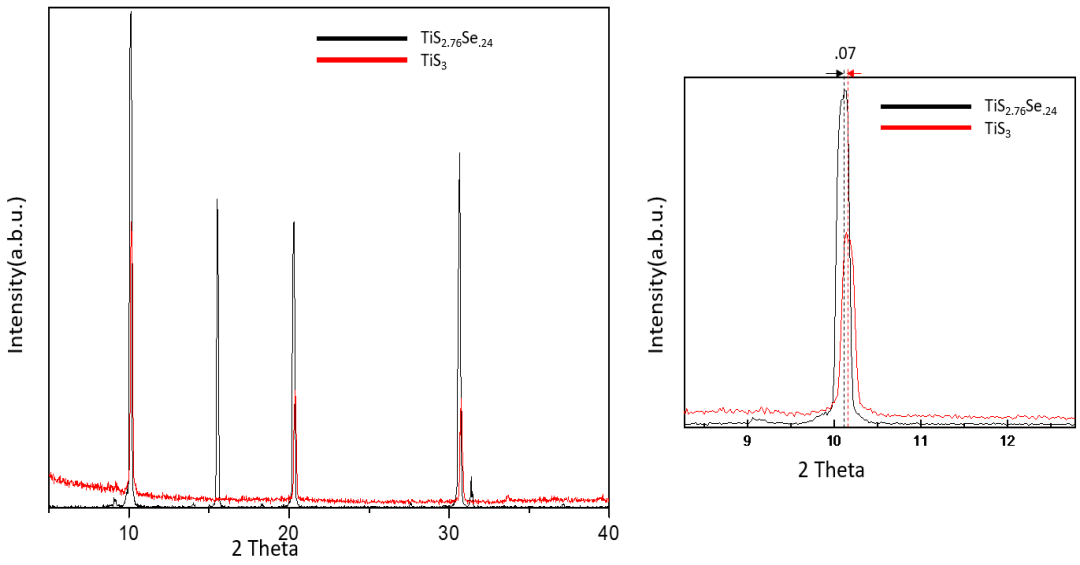

Figure 4-3 Left, XRD spectrum of $TiS_{2.76}Se_{.24}$ and its comparison with TiS_3. Right, zoomed in view of one of the peak to show deviation in $TiS_{2.76}Se_{.24}$ from TiS_3

4.5 Energy dispersive X-ray Spectroscopy (EDX)

Qualitative Elemental analysis was performed on CVT grown crystal using EDX on SEM and TEM. Figure 4-4 shows the presence of titanium, sulfur and selenium confirm the alloying behavior of $TiS_{3(1-x)}$ Se_{3x}. From the compositional analysis value of x comes out to be .08.

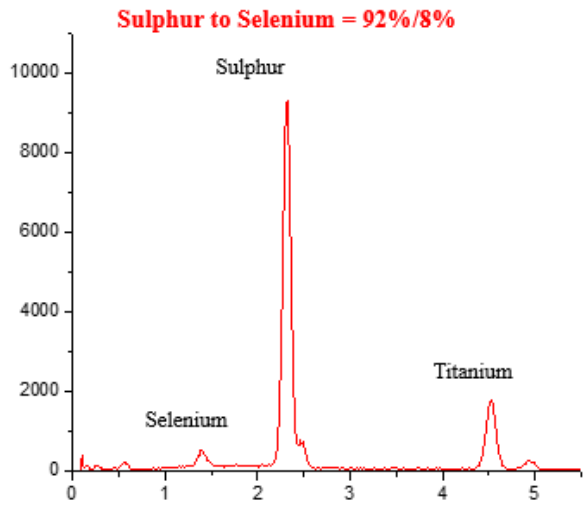

Figure 4-4 EDX spectrum of $TiS_{2.76}Se_{.24}$ showing presence of selenium, sulfur and titanium

4.6 Raman Spectroscopy

As discussed in the first chapter, 4 Raman active vibrational modes can be observed for TiS_3. Typical Raman spectra for $TiS_{2.76}Se_{.24}$ alloy is shown in figure 4-5 and its comparison with TiS_3. As shown in figure 4-5, the vibrational nature of this alloy is like the TiS_3 except there is red shift in the alloy owing to the higher mass of selenium atom. We also saw a new peak in the alloy at 450cm^{-1}. This peak corresponds to sulfur to selenium vibration that was reported in $HfS_{3-x}Se_x$ and $ZrS_{3-x}Se_x$ [65,66]. Peak at 521cm^{-1} in $TiS_{2.76}Se_{.24}$ and TiS_3 corresponds to peak shown by silicon. As shown in table 4-1, careful analysis of Raman peaks has also been done by calculating full width half maximum (FWHM), and there is significant increase in FWHM percentage. This increase is attributed to defects created by alloying the selenium into TiS_3.

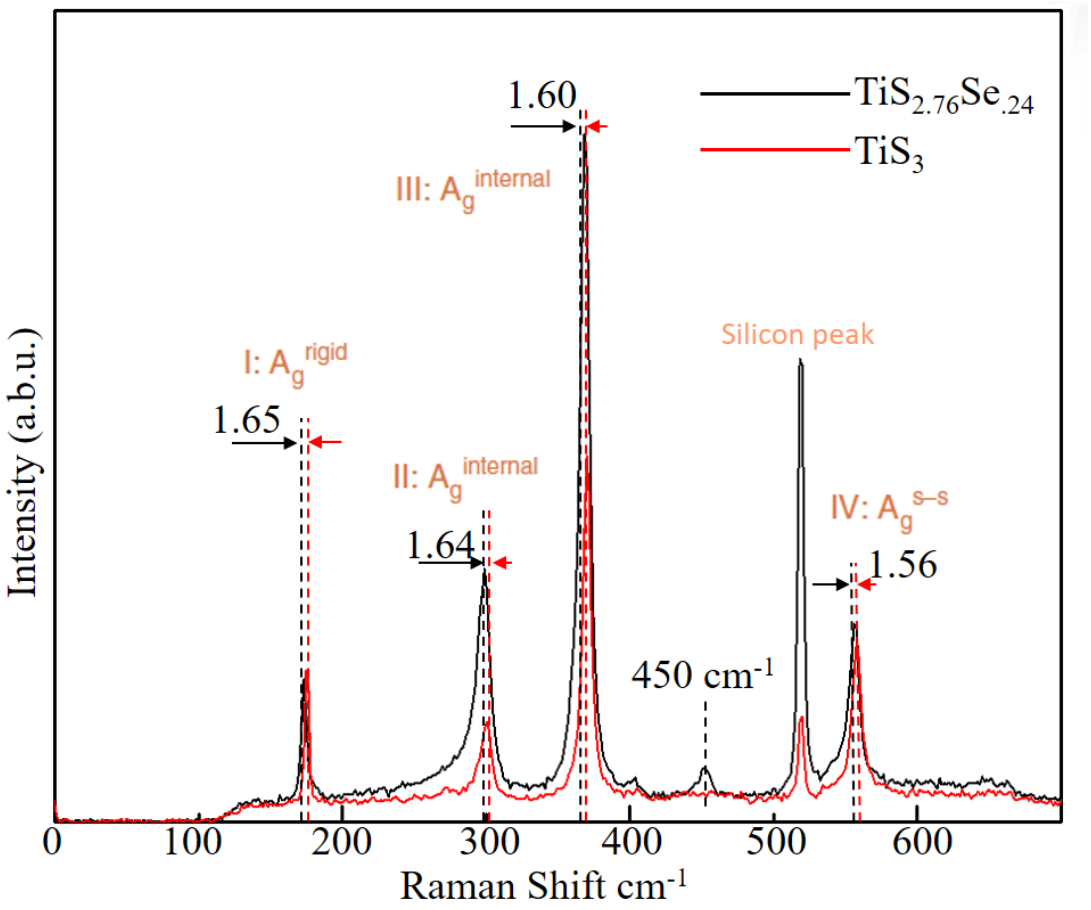

Figure 4-5 Raman spectrum of $TiS_{2.76}Se_{.24}$ and its comparison with TiS_3

Table 4-1 Full width half maximum of Raman peaks of $TiS_{2.76}Se_{.24}$ and its comparison with TiS_3

Peak	TiS_3(cm^{-1})	$TiS_{2.76}Se_{.24}$(cm^{-1})	% change in FWHM
176 like peak	3.65	4.62	26.5%

300 like peak	9.45	11.2	18.5%
370 like peak	6.96	8.1	16.3%
557 like peak	7.59	11.26	48.3%

4.7 Angle Resolved Raman Spectroscopy

Same setup described in chapter 2 has been used to measure anisotropy of $TiS_{2.76}Se_{.24}$. We took our measurements in the normal configuration, where incident light is parallel to detection. We took all the measurement in an interval of 15 degree at the same spot with very little laser power to avoid sample burning. The main aim of this study is to identify characteristic peak to identify chain direction in the alloy; and to study its comparison with TiS_3. As shown in figure 4-3 the anisotropy direction is very similar to TiS_3 and chain direction can be identified using $370cm^{-1}$ like TiS_3 peak.

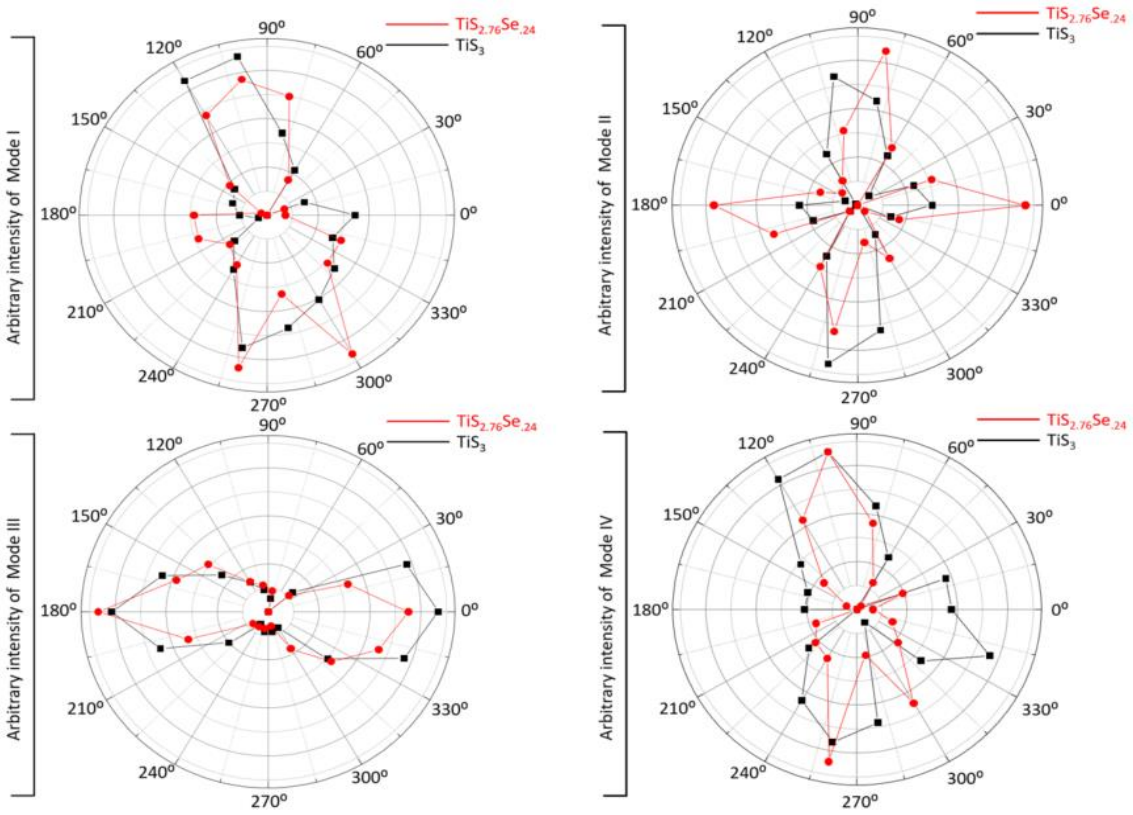

Figure 4-6 Polar plot of Raman active peaks of $TiS_{2.76}Se_{.24}$ and its comparison with TiS_3

Chapter 5 Conclusion and Future Scope

5.1 Introduction

The full potential of 2D materials is limited only by number of 2D materials that can be commercially manufactured. Concurrently, properties of existing materials can be further tuned in many ways like thermal annealing, strain engineering, defect introduction and alloying. Among them alloying has proved to be the most efficient way to utilize full potential of 2D materials. Till date, extensive studies on 2D alloys of isotropic materials have been performed. In this work we have focused on alloys of anisotropic materials. We have theorized and experimentally demonstrated alloys of ReS_2 & $ReSe_2$ from TMDCs and TiS_3 & $TiSe_3$ from TMTCs.

5.2 Growth

5.2.1 ReS_2 & $ReSe_2$

Both CVT and CVD method have been demonstrated for alloying this material. ReSSe has been obtained using CVT by sealing its constituent element in quartz ampoule at low pressure and temperature ramped up to 1050°C. Crystals were exfoliated onto Si/SiO_2 substrate for detailed characterization.

Large area alloy of ReSSe have also been demonstrated using chemical vapor deposition techniques. It was grown on sapphire substrate using ammonium perhnate, sulfur and selenium placed in quartz boat at temperatures up to 500°C. Sulfur and Selenium was transferred to substrate using inert gas. Morphology of grown film is in shape of hexagon and truncated triangle. These samples were stored in vacuum for further studies.

5.2.2 TiS_3 & $TiSe_3$

Chemical vapor transport was used to grow this crystal. Titanium sheet accompanied with sulfur and selenium pallets were sealed in quartz ampoule with iodine as transport agent. Ampoule was placed at 550°C with gradient of 450°C for 5 days. Crystal of $TiS_{2.76}Se_{.24}$ was grown in whiskers form and exfoliated on Si/SiO_2 substrate for further characterization.

As per convex Hall curve, adding selenium to TiS_3 can from stoichiometric compound only at concentration of selenium below 1/3. In figure x-axis is selenium concentration in TiS_3 and y-axis is for reference. Composition lies on the blue curve (convex Hall curve) or near to it is the favorable case. Also, as per figure 5-1, TiS_2Se is the most favorable composition. This discrepancy in theory and experimental calculation can be attributed to low Vander Waals interaction consideration in theory as compared to experimental results.

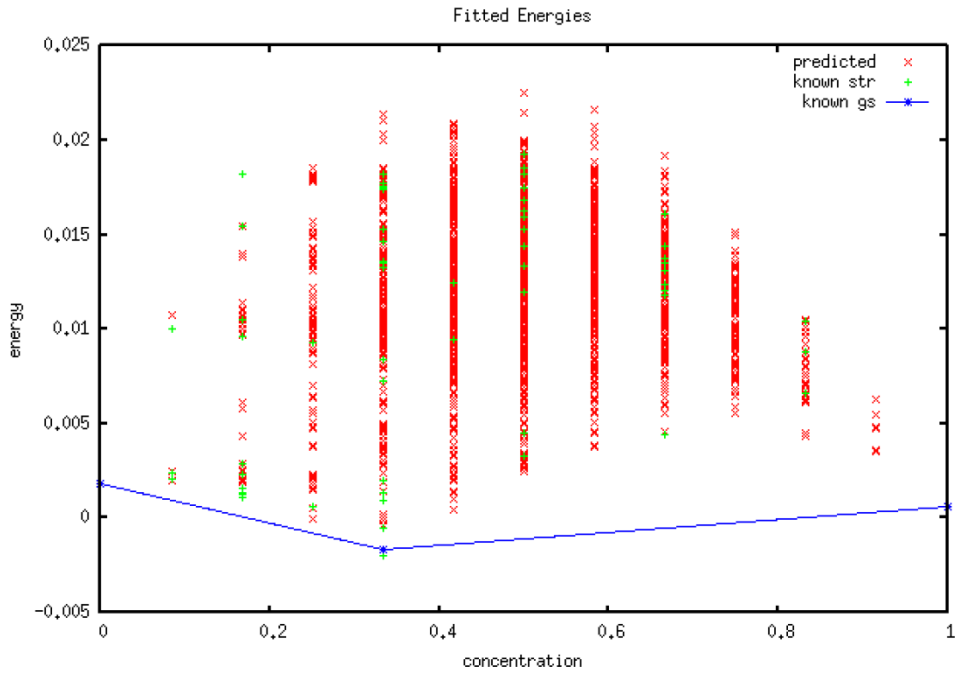

Figure 5-1 Theoretically calculated Convex hall curve for alloy of TiS_3 and TiSe3, showing the most favorable composition

5.3 Characterization

Elemental analysis was done using EDX spectroscopy in SEM. For ReSSe, sulfur and selenium composition comes out to be 1:1 and for $TiS_{3(1-x)}Se_{3(x)}$, x comes out to be .08. Crystal structure was further confirmed by XRD and TEM. Since anisotropic, both alloys crystallize in 1D chain like structure. Band gap of exfoliated ReSSe comes out to be 1.39eV using photoluminescence. Also, Raman spectroscopy was used to study vibrational nature and anisotropy direction for both the alloys. Raman peaks for identifying chain direction/b-axis were successfully identified for both alloys.

5.4 Conclusion

Alloys of 2D anisotropic TMDCs and 2D TMTCs have been successfully demonstrated using CVT and CVD. Angle dependent Raman measurements confirm the in-

plane anisotropy of both the alloys. Also, band gap tuning was demonstrated using photoluminescence by measuring band gap of ReSSe alloy. Alloy of TMTCs have been demonstrated using CVT method, but scalable growth needs to be achieved to exploit its full potential in industries. Although CVD of ReSSe has been demonstrated, the anisotropy still comes out to be finite and with a very weak anisotropic ratio. Research needs to be directed over this to control the anisotropic direction to get long range order anisotropy.

5.5 Future Work

The benefits of pseudo 1D materials can only translate into the real world by enabling their large-scale manufacture with controlled anisotropy. Without this, these materials cannot be used at device level because of loss of anisotropy due to random orientation of chain or finite anisotropy as discussed in section 3.11 & 3.12. Controlled growth of anisotropy can be achieved by step edge growth. Bin et.al [64] show controlled ReS_2 growth on the edges of WS_2, having anisotropy perpendicular to the edges of WS_2 as shown in figure.

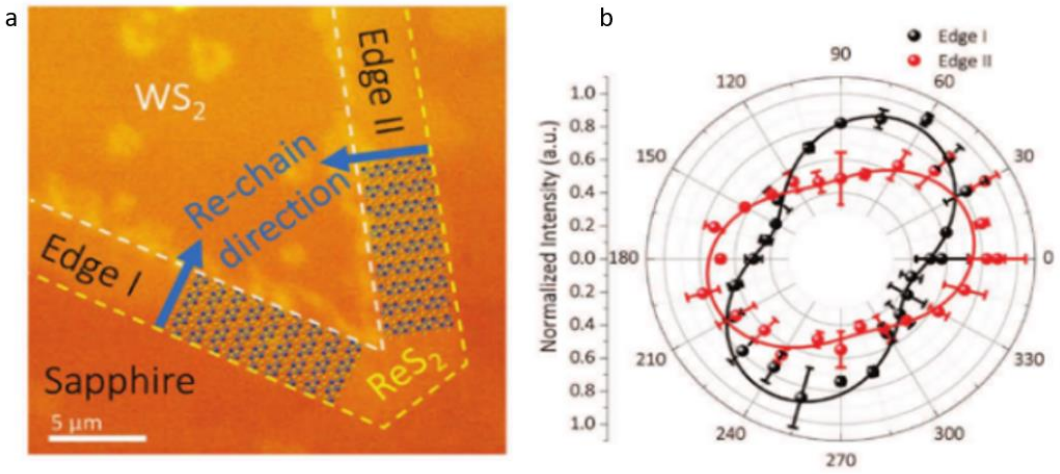

Figure 5-2 a] ReS_2 grown on the edges of WS_2 with chain direction perpendicular to the edges b] Polar plot of the ReS_2 showing chain direction at the edge I and II [64]

5.5.1 Preliminary studies

Based on this experience we tried controlled growth of ReS_2 on sapphire substrate. Terraces were created on c cut sapphire by annealing to 1500°C for 3 hrs. under hydrogen environment. Figure 5-3 shows the AFM images of sapphire after treatment with the steps created on it. Step edges of a few nanometers have been created using this technique.

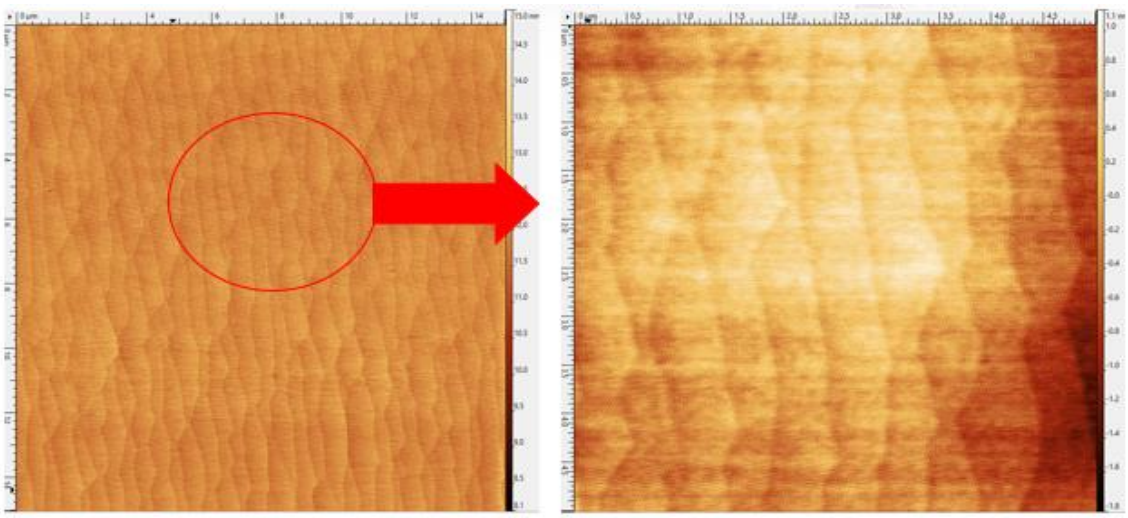

Figure 5-3 AFM images showing terraces on sapphire substrate, (right) shows zoomed in view of these terraces

ReS_2 was grown using CVD technique on these surfaces reconstructed sapphire substrate. Prior to growth, treated sapphire was cleaned using IPA and DI water and blowing it with dry nitrogen. Then the substrate was loaded into CVD chamber with NH_4ReO_4 and sulfur at 500°C for 15minutes. Chamber will cool down naturally after the growth. Images of as grown ReS_2 were captured using optical microscope. As shown in figure 5-4a,b, morphology of CVD grown ReS_2 on surface reconstructed sapphire is completely different from growth on non-treated sapphire. ReS_2 grown on treated sapphire looks to have a Nano-ribbon like structure which is strong signal of controlled anisotropy growth.

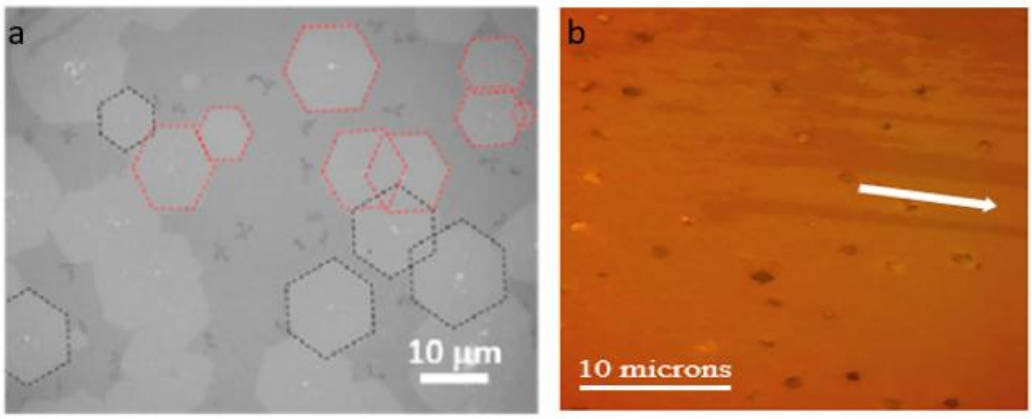

Figure 5-4 a] Optical image of CVD grown ReS_2 on non-treated sapphire substrate b] Optical image of CVD grown ReS_2 on surface reconstructed sapphire

When grown, film was confirmed using Raman spectrum shown in figure, which is same as previously reported by Kedi.et.al [50].

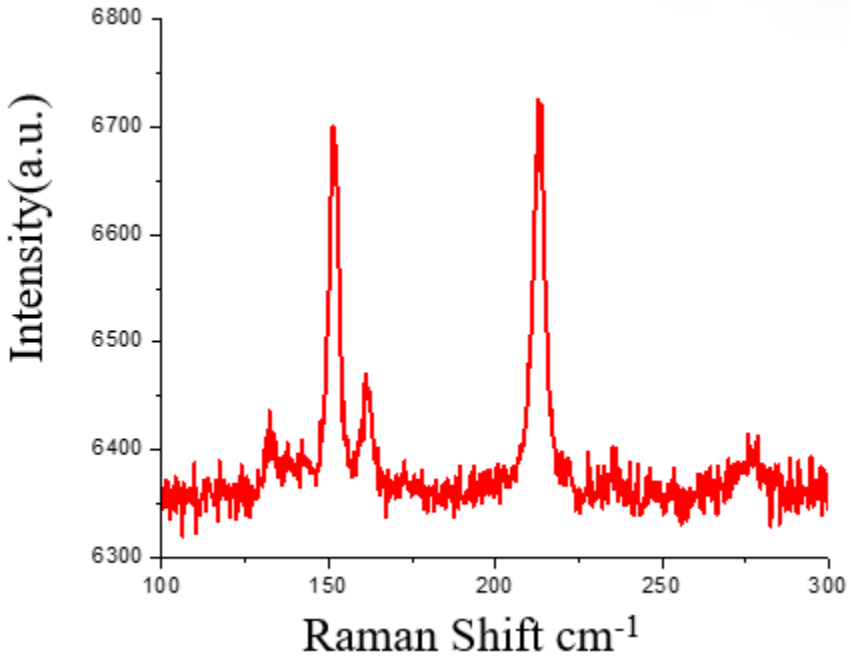

Figure 5-5 Raman spectrum of CVD grown ReS_2 on surface reconstructed sapphire substrate

Preliminary study on surface morphology and anisotropy direction were performed using AFM and angle dependent Raman measurement as shown in figure 5-6a and 5-6b respectively. Angle dependent Raman was performed at normal configuration explained in chapter 2 with zero angle corresponds to shown in inset of figure 5-6b. We plotted mode V peaks which corresponds to Re-Re vibrations.

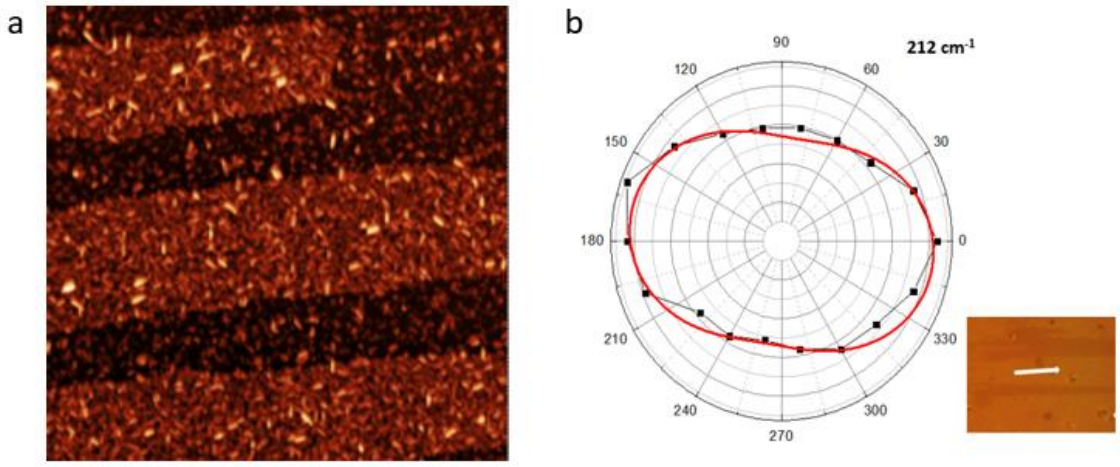

Figure 5-6 a] AFM image of CVD grown ReS_2 on sapphire terraces b] Polar plot of ReS_2 grown on sapphire terraces using CVD

As shown in figure 5-6(a-b), anisotropy of the film is very weak and AFM images indicates very rough film. We are working on improving anisotropy by controlling growth parameters and increasing the height and width of step sizes.

References

1. L. D. Landau and E. M. Lifshitz, Statistical Physics, Part I &II, Pergamon Press, Oxford, 1980.

2. R. E. Peierls, Ann. Inst. Henri Poincare, 1935, 5, 177–222.

3. R. E. Peierls, Helv. Phys. Acta, 1934, 7, 81–83.

4. Mermin N D and Wagner H 1966 Phys. Rev. Lett. 17 1133–6

5. Novoselov K S, Geim A K, Morozov S V, Jiang D, Zhang Y, Dubonos S V, Grigorieva I V and Firsov A A 2004 Science 306 666–9

6. Cassabois G, Valvin P and Gil B 2016 Nat. Photon.10 262–6

7. Pacil D, Meyer J C, Girit C and Zettl A 2008 Appl. Phys. Lett. 92 133107

8. Splendiani A, Sun L, Zhang Y, Li T, Kim J, Chim C Y, Galli G and Wang F 2010 Nano Lett. 10 1271–5

9. Tang, Qing, and Zhen Zhou. "Graphene-analogous low-dimensional materials." Progress in Materials Science 58.8 (2013): 1244-1315

10. Paul, J. T., et al. "Computational methods for 2D materials: discovery, property characterization, and application design." Journal of Physics: Condensed Matter 29.47 (2017): 473001.

11. Geim AK, Novoselov KS. The rise of graphene. Nat Mater 2007;6:183–91.

12. Novoselov, Konstantin S., et al. "Room-temperature quantum Hall effect in graphene." Science 315.5817 (2007): 1379-1379.

13. Eda, G., Fanchini, G., and Chhowalla, M., Large-area ultrathin films of reduced graphene oxide as a transparent and felxible electronic material. Nature Nanotechnology doi:10.1038/nnano.2008.83 (2008).

14. Hernandez, Yenny, et al. "High-yield production of graphene by liquid-phase exfoliation of graphite." Nature nanotechnology 3.9 (2008): 563-568.

15. Kim, Keun Soo, et al. "Large-scale pattern growth of graphene films for stretchable transparent electrodes." nature 457.7230 (2009): 706-710

16. Han, Melinda Y., et al. "Energy band-gap engineering of graphene nanoribbons." Physical review letters 98.20 (2007): 206805.

17. Ni, Zhen Hua, et al. "Uniaxial strain on graphene: Raman spectroscopy study and band-gap opening." ACS nano 2.11 (2008): 2301-2305.

18. Zhou, S. Yi, et al. "Substrate-induced bandgap opening in epitaxial graphene." Nature materials 6.10 (2007): 770-775

19. Zeng, Haibo, et al. "'White graphenes": boron nitride nanoribbons via boron nitride nanotube unwrapping." Nano letters 10.12 (2010): 5049-5055.

20. Kaul, Anupama B. "Two-dimensional layered materials: Structure, properties, and prospects for device applications." Journal of Materials Research 29.3 (2014): 348-361.

21. Watanabe, Kenji, Takashi Taniguchi, and Hisao Kanda. "Direct-bandgap properties and evidence for ultraviolet lasing of hexagonal boron nitride single crystal." Nature materials 3.6 (2004): 404-409.

22. Kim, Ki Kang, et al. "Synthesis of monolayer hexagonal boron nitride on Cu foil using chemical vapor deposition." Nano letters 12.1 (2011): 161-166.

23. Shi, Yumeng, et al. "Synthesis of few-layer hexagonal boron nitride thin film by chemical vapor deposition." Nano letters 10.10 (2010): 4134-4139.

24. Radisavljevic B, Radenovic A, Brivio J, Giacometti V, Kis A. Single-layer MoS2 transistors. Nat Nanotechnol 2011;6:147–50.

25. Verble, J. L., and T. J. Wieting. "Lattice Mode Degeneracy in Mo S 2 and Other Layer Compounds." Physical review letters 25.6 (1970): 362.

26. Frey, G. L., et al. "Optical-absorption spectra of inorganic fullerenelike M S 2 (M= Mo, W)." Physical Review B 57.11 (1998): 6666.

27. P. Tao, H. Guo, T. Yang, and Z. Zhang, Strain-induced magnetism in MoS2 monolayer with defects, J. Appl. Phys.115(5), 054305 (2014)

28. Yoon, Youngki, Kartik Ganapathi, and Sayeef Salahuddin. "How good can monolayer MoS2 transistors be?." Nano letters 11.9 (2011): 3768-3773.

29. Heising, Joy, and Mercouri G. Kanatzidis. "Exfoliated and restacked MoS2 and WS2: Ionic or neutral species? Encapsulation and ordering of hard electropositive cations." Journal of the American Chemical Society 121.50 (1999): 11720-11732.

30. Kim, Yun, Jin-Lin Huang, and Charles M. Lieber. "Characterization of nanometer scale wear and oxidation of transition metal dichalcogenide lubricants by atomic force microscopy." Applied physics letters 59.26 (1991): 3404-3406.

31. Zong, Xu, et al. "Enhancement of photocatalytic H2 evolution on CdS by loading MoS2 as cocatalyst under visible light irradiation." Journal of the American Chemical Society 130.23 (2008): 7176-7177.

32. Van Schalkwijk, Walter, and Bruno Scrosati. "Advances in Lithium Ion Batteries Introduction." Advances in Lithium-Ion Batteries. Springer, Boston, MA, 2002. 1-5.

33. Wang, Qing Hua, et al. "Electronics and optoelectronics of two-dimensional transition metal dichalcogenides." Nature nanotechnology 7.11 (2012): 699.

34. Das, Saptarshi, et al. "High performance multilayer MoS2 transistors with scandium contacts." Nano letters 13.1 (2012): 100-105.

35. Ting, Louisa Rui Lin, et al. "Catalytic activities of sulfur atoms in amorphous molybdenum sulfide for the electrochemical hydrogen evolution reaction." ACS Catalysis 6.2 (2016): 861-867.

36. Dai, Jun, Ming Li, and Xiao Cheng Zeng. "Group IVB transition metal trichalcogenides: a new class of 2D layered materials beyond graphene." Wiley Interdisciplinary Reviews: Computational Molecular Science 6.2 (2016): 211-222.

37. Island, Joshua O., et al. "Electronics and optoelectronics of quasi-1D layered transition metal trichalcogenides." 2D Materials 4.2 (2017): 022003.

38. Tongay, Sefaattin, et al. "Monolayer behaviour in bulk ReS 2 due to electronic and vibrational decoupling." Nature communications 5 (2014): 3252.

39. Hafeez, Muhammad, et al. "Rhenium dichalcogenides (ReX 2, X= S or Se): an emerging class of TMDs family." Materials Chemistry Frontiers 1.10 (2017): 1917-1932.

40. Chenet, Daniel A., et al. "In-plane anisotropy in mono-and few-layer ReS2 probed by Raman spectroscopy and scanning transmission electron microscopy." Nano letters 15.9 (2015): 5667-5672.

41. Jariwala, Bhakti, et al. "Synthesis and characterization of ReS2 and ReSe2 layered chalcogenide single crystals." Chemistry of Materials 28.10 (2016): 3352-3359.

42. Wolverson, Daniel, et al. "Raman spectra of monolayer, few-layer, and bulk ReSe2: An anisotropic layered semiconductor." Acs Nano 8.11 (2014): 11154-1116

43. Hafeez, Muhammad, et al. "Chemical vapor deposition synthesis of ultrathin hexagonal rese2 flakes for anisotropic raman property and optoelectronic application." Advanced Materials 28.37 (2016): 8296-8301.

44. Wen, Wen, et al. "Anisotropic Spectroscopy and Electrical Properties of 2D ReS2 (1–x) Se2x Alloys with Distorted 1T Structure." small 13.12 (2017).

45. Ferrer, I. J., Macia´, M. D., Carcele´n, V., Ares, J. R. & Sa´nchez, C. On the photoelectrochemical properties of TiS3 films. Energy Proc. 22, 48–52 (2012).

46. Ferrer, I. J., Ares, J. R., Clamagirand, J. M., Barawi, M. & Sa´nchez, C. Optical properties of titanium trisulphide (TiS3) thin films. Thin Solid Films 535, 398–401 (2013)

47. Dai, J. & Zeng, X. C. Titanium trisulfide monolayer: theoretical prediction of a new direct-gap semiconductor with high and anisotropic carrier mobility.

48. Angew. Chem. Int. Ed. 54, 7572–7576 (2015).18. Molina-Mendoza, A. J. et al. Electronic bandgap and exciton binding energy of layered semiconductor TiS3. Adv. Electron. Mater. 1, 1500126 (2015).

49. Kong, Wilson, et al. "Angle resolved vibrational properties of anisotropic transition metal trichalcogenide nanosheets." Nanoscale 9.12 (2017): 4175-4182.

50. Wu, Kedi, et al. "Unusual lattice vibration characteristics in whiskers of the pseudo-one-dimensional titanium trisulfide TiS 3." Nature communications 7 (2016): 12952.

51. da Rocha Martins, J.; Chacham, H. Disorder and Segregation in B−C−N Graphene-Type Layers and Nanotubes: Tuning the Band Gap. ACS Nano 2011, 5, 385−93.

52. Yuge, K. Phase Stability of Boron Carbon Nitride in a Heterographene Structure: A First-Principles Study. Phys. Rev. B 2009, 79, 144109.

53. Komsa, Hannu-Pekka, and Arkady V. Krasheninnikov. "Two-dimensional transition metal dichalcogenide alloys: stability and electronic properties." The journal of physical chemistry letters 3.23 (2012): 3652-3656.

54. Kobayashi, Yu, et al. "Bandgap-tunable lateral and vertical heterostructures based on monolayer Mo1-xWxS2 alloys." Nano Research 8.10 (2015): 3261-3271.

55. Tongay, Sefaattin, et al. "Two-dimensional semiconductor alloys: Monolayer Mo1−xWxSe2." Applied Physics Letters104.1 (2014): 012101.

56. Kang, Jun, et al. "Monolayer semiconducting transition metal dichalcogenide alloys: Stability and band bowing." Journal of Applied Physics 113.14 (2013): 143703.

57. Xie, L. M. "Two-dimensional transition metal dichalcogenide alloys: preparation, characterization and applications." Nanoscale 7.44 (2015): 18392-18401.

58. Cui-Huan, Ge, et al. "Band gap engineering of atomically thin two-dimensional semiconductors."

59. Zhang, Qi, Daniel Sando, and Valanoor Nagarajan. "Chemical route derived bismuth ferrite thin films and nanomaterials." Journal of Materials Chemistry C 4.19 (2016): 4092-4124.

60. Butler, Holly J., et al. "Using Raman spectroscopy to characterize biological materials." Nature protocols 11.4 (2016): 664.

61. Ho, C. H., et al. "Crystal structure and band-edge transitions of ReS2− xSex layered compounds." Journal of Physics and Chemistry of Solids 60.11 (1999): 1797-1804

62. Wachter, S., et al. "Relaxation of localized excitons in CdSe/ZnSe heterostructures containing quantum islands of different sizes." Physica Status Solidi B Basic Research 224.2 (2001): 437-441.

63. Feng, Yanqing, et al. "Raman vibrational spectra of bulk to monolayer Re S 2 with lower symmetry." Physical Review B92.5 (2015): 054110.

64. Chen, Bin, et al. "Controlling Structural Anisotropy of Anisotropic 2D Layers in Pseudo-1D/2D Material Heterojunctions." Advanced materials 29.34 (2017).

65. Zwick, A., et al. "Raman scattering in the ternary phase Hf S 3− x Se x." Physical Review B 26.10 (1982): 5694.

66. Zwick, A., et al. "Phonons in the ternary phase ZrS3-xSex." Solid State Communications 45.10 (1983): 889-893.